UNIVERSITY OF CALIFORNIA

SANTA CRUZ

COMBINING FIRST-PRINCIPLES DENSITY FUNCTIONAL THEORY CALCULATIONS WITH EXPERIMENTAL APPROACHES TO UNDERSTAND THE IMPACTS OF DOPING ON THE ELECTRICAL CONDUCTIVITIES OF HEMATITE

A dissertation submitted in partial satisfaction

of the requirements for the degree of

DOCTOR OF PHILOSOPHY

in

CHEMISTRY

by

Mingpeng Chen

June 2022

The Dissertation of Mingpeng Chen is approved:

_____

Professor Yat Li, Chair

_____

Professor Jin Zhong Zhang

_____

Professor Yuan Ping

_____

Peter F. Biehl

Vice Provost and Dean of Graduate Studies

Table of Contents

List of Figures

Chapter 1

Chapter 2

List of Tables

Chapter 2

Chapter 3

Abstract

Combining First-principles Density Functional Theory Calculations with Experimental Approaches to Understand the Impacts of Doping on the Electrical Conductivities of Hematite

by

Mingpeng Chen

Hematite is a promising material for many different energy conversion and storage applications due to advantages such as low cost, high abundance, and good chemical stability. However, the low electrical conductivity of hematite has hindered the wide application of hematite in for different applications. Atomic doping is one of the most used approaches to tackle the electrical conductivity problem in hematite. Although many works have been done to understand the effects of atomic doping to the electrical conductivity of hematite, there are still many questions not answered yet. In this dissertation, we couple first-principles density functional theory (DFT) calculations with experimental approaches to dive deep into the system and answer unsolved questions in the community by taking advantages of both approaches. We, first of all, employ first-principles DFT calculations to predict how atomic doping impacts the carrier concentrations, carrier mobility and electrical conductivity of hematite. Then we conduct experiments to verify previous predicted results starting from materials synthesis, then materials characterizations, and, in the end, performance measurement. This series of works deepen people's understanding about how atomic

doping impacts the electrical conductivities of hematite and provide a possible validated collaboration mode between first-principles DFT calculations and experimental approaches.

Dedication

DEDICATED

TO

MY FAMILY, MY ADVISOR, MY FRIENDS, AND EVERYONE WHO HAS

HELPED ME

Acknowledgements

Time flies, it has been five years since I came to Santa Cruz. I remember that, back then, graduate programs advisor is still Janet. The day when I came to UCSC for campus visiting, she showed me around the campus. I was immediately impressed by the beauty of the campus. From then on, I fell in love with this campus. During the past five years, whenever I feel tired, I like to walk around the campus. The grassland near OPERS is always my favorite and the view over there is incredible and never let me down.

At this point, I am near finishing my PhD program, and I would like to take the chance to thank my parents, my advisor, my friends and everyone who have helped me. Without your support, I cannot make it all the way to here.

I would like to thank my parents for giving me the opportunity to come to US to do my PhD. I know that many people do not have the opportunity to go abroad to study, therefore, I am very thankful. My parents have also been very supportive whenever I need help from them.

I would like to thank my advisor, Yat Li. He has been patiently instructing me how to do research in the past 5 years. When my research is not going well, he did not blame me, instead, he is always actively thinking about what we can do to solve problems. In addition, I appreciate Yat for allowing me to explore different things I am interested in, such as simulation. I thank Prof. Yuan Ping for teaching me how to do simulation and how to think as a theorist. Her careful attitude in work has made me a better researcher. I really appreciate that. Prof. Jin Zhong Zhang gave me a lot of good

suggestions during my research milestone, I also really appreciate that. Dr. Tao Cheng is another person that teaches me a lot of simulation skills. Without his help and instruction, I cannot finish the “pH dependent of N-doped carbon project”. Fang also gave me a lot of support during my PhD. When my research is not going well, she gave me a lot of encouragement.

I would like to thank Dr. Feng Wu and Dr. Tyler J. Smart. They are the people who teach me how to do simulation hand by hand. I have learned so much from them. I still remember that the first day when I started to learn simulation, Feng patiently taught me how to use Vim. There are so many times that we worked together in the lab until 10 or 11 pm then left lab together. These memories are valuable for me. Tyler also taught me a lot when we worked together on the hematite project. Without his help, I cannot make so much progress on this project.

I would like to thank my other lab mates, Shanwen Wang, Dun Lin, Xinzhe Xue, Qiu Ren, Dr. Bin Yao, Dr. Tianyi Kou, Megan Freyman, Anica Pinongcus, Sam Eisenberg, Adam Carleton, Po Ching Hsu (Eric), Frances Li, Dr. Cheng Cheng, Dr. Huarong Peng, Dr. Xiaoli Fan, Dr. Dewei Rao, Dr. Lei Zhang. They also helped a lot in my research in the past 5 years.

I would like to thank our collaborators, Bud Bridges, Andrew Grieder, Valentin Urena Baltazer, Gongming Wang, Mingzhao Liu, Chenyu Zhou.

I would like to thank my friends for all the help during job search: Wangyuan Zeng, Hongliang Shi, Shiyun Huang, Jianfeng Shi, Jie Yin, Jincheng Li, Pengyang

Zhou, Mengqing Wang, Yu Zhang, Liting Feng, Xingjian Jiang, Zhenzhuo Lan, Philip Lin, Yaohua Guo. Without your help, I cannot find my job.

I would like to thank my friends for hanging out with me in my free time, Yan Zhang, Yufei Shan, Yunzhe Li, Xiaotian Zheng, Xiaoyi Guo, Jinghui Geng, Jinghong Zhang, Yannong He, Yang Xiang, Ge Zhang, Yaodong Xu, Guanghong Xu, Yiluan Song, Qiuxia Tang, Qiming Liu, Xinyun Cui, Peng Zhou, Nan Wang, Jing Xiong, Dongran Zhai, Bingzhang Lu, Shijun Sun, Yue Ma, Po-Chun Chung, Kejun Li, Chunhao Guo, Chunyi Zhao. My life becomes more colorful because of you.

I would like to thank my landlord, Jennifer Clear, Braulio Clear and their son Rico. They really helped me a lot when I first came to Santa Cruz. I had such a great time living there in the first three years of living in Santa Cruz.

I would like to thank everyone who has helped in the past five years.

In the end, I would like to say the past five-years in Santa Cruz is one of the most memorable days of my life, not only I learned so much knowledge, but also grew up so much as an individual. Although the knowledge I learned in the past several years might not be used in my future work, the determination, patience, critical thinking I learned in the process will benefit me forever.

The text of this dissertation includes reprints of the following previously published materials:

1. **Chen, M.** †, Grieder, A. † (equal contribution), Smart, T.J., Li, Y. and Ping, Y. The effect of dopants on the carrier mobility of hematite. In preparation.
2. T. J. Smart, **M. Chen** † (equal contribution), A. C. Grieder, V. Urena Baltazar, F. Bridges, Y. Li, and Y. Ping, J. Appl. Phys. 130, 245705 (2021)
3. T. J. Smart, V. U. Baltazar, **M. Chen**, B. Yao, K. Mayford, F. Bridges, Y. Li, and Y. Ping, Chem. Mater. 33, 4390 (2021)
4. **M. Chen,** T. J. Smart, S. Wang, T. Kou, D. Lin, Y. Ping, and Y. Li, J. Mater. Chem. A 8, 8783 (2020)
5. T. Kou, **M. Chen**† (equal contribution), F. Wu, T. J. Smart, S. Wang, Y. Wu, Y. Zhang, S. Li, S. Lall, Z. Zhang, Y.-S. Liu, J. Guo, G. Wang, Y. Ping, and Y. Li, Nat. Commun. 11, 590 (2020)

Chapter 1 – Introduction

Abstract

Hematite is an attractive material for many energy storge and conversion applications due to its advantages such as low cost, high abundance, good chemical stability However, the wide application of hematite is hindered by the poor electrical conductivity of hematite, which is originating from polaron formation. Atomic doping is one of the most promising approaches to improve the electrical conductivities of hematite. Although many works have been done to understand the effect of atomic doping, there are still many questions not well answered yet. Since first-principles density functional theory (DFT) calculation could help get insights into the structural and electronic information of materials, we coupled it with experimental approaches and systematically studied how atomic doping impacts the electrical conductivities of hematite from several different perspectives such as clustering, carrier concentrations and carrier mobilities. The coupling of first-principles DFT calculations with experimental approaches deepens our understanding of how doping impacts the electrical conductivities of hematite and provides guidance on how to choose suitable dopants to optimize the performance of hematite-based device.

1.1 Introduction to Hematite and Polaron

Hematite ($\alpha - Fe_2O_3$) is the most stable oxide of Fe and is widely found in rocks and soils in nature. The density is 5.3 g/cm^3 and the color is usually red. It has a hexagonal crystal structure with an experimental lattice constant of a = 5.038 Å, c = 13.772 Å. Among all possible intrinsic defects of hematite such as O vacancies, Fe interstitials, etc., O vacancies have the lowest formation energy. Since O vacancies donate free electron carriers, hematite is an intrinsic n-type semiconductor.[1,2]

When the extra free electrons interact with the crystal lattice of hematite, i.e., repelled by negatively charged O ions and attracted by positively charged Fe ions, the strong electron-phonon interaction localizes electron at one specific Fe site. The quasi-particle, including an electron dressed by a cloud of virtual phonons, is called electron polaron. Instead, if a hole is localized on an O ion, the formed quasi-particle is called hole polaron. Since hematite is an intrinsic n-type semiconductor, we will only discuss electron polaron for the rest of this dissertation. Depending on the spatial extent of the polarization cloud, the polaron can be divided into small polarons and large polarons, depending on the size of the electron-phonon interaction. Small polaron is usually used to describe the short-range electron-phonon interaction, with a polaron radius around lattice constant. The characteristics include (1) narrow and flat mid-gap electronic state below the Fermi level, (2) thermally activated hopping mobility with a value much smaller than 1 cm^2 V^{-1} s^{-1}, which increases with temperature. Conversely, the electron-phonon interaction range of large polarons is much larger, with a polaron radius much larger than lattice constant. Large polarons have free carrier mobility much larger than

1 cm^2 V^{-1} s^{-1}, which decreases with temperature. The different mobility-temperature dependence for small and large polarons is due to the different mechanisms of charge transport in the material. Small polarons are likely to undergo phonon-assisted hopping, because the charge carrier localization is destabilized by the thermally induced atomic distortions around the trapping site, resulting in occasional hopping. On the other hand, for large polarons, the reason that the mobility increases with temperature is owing to the enhanced thermal distortions. In contrary to small polarons, large polarons tend to sustain a free-carrier-like coherent motion. The large effective mass of the large polarons determines a high mobility, as it preserves the polaron motion from occasional scattering with the phonon field, and the fact that the large polaron mobility decreases with temperature is because the scattering becomes more effective.[3]

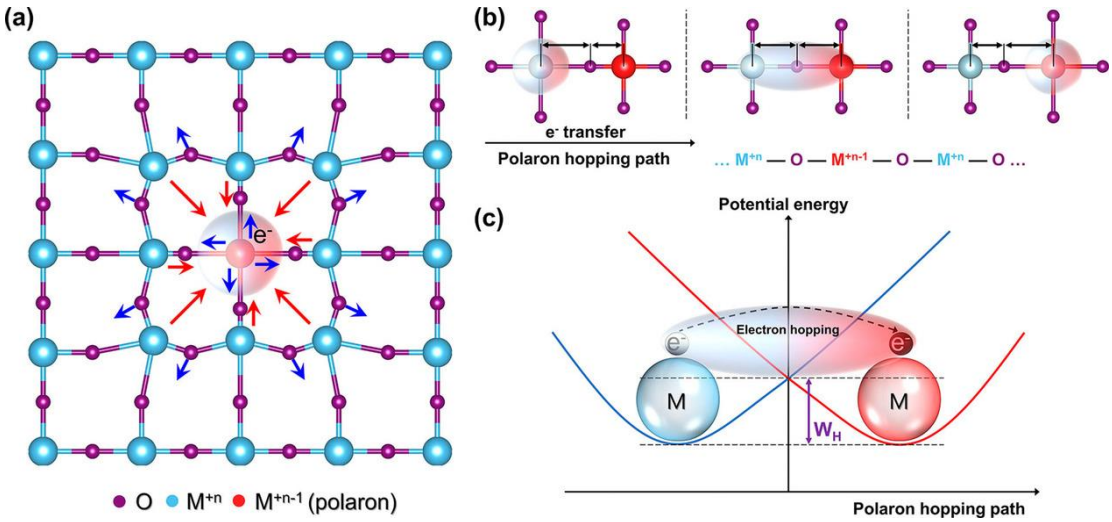

Figure 1.1 A schematic illustration of a small polaron in a transition metal oxide (TMO) lattice. (a) Polarization induced by localization of an electron at a lattice site and formation of a small polaron. Red and blue arrows represent attractive and repulsive

forces, respectively. (b) Lattice deformation along the polaron hopping path, illustrating the change of bond lengths due to Coulombic force induced by the electron charge. (c) Energy diagram of the electron transfer between the variable-valence metal ions (M) via an intermediate oxygen. W_H reflects the energy required to produce the geometric configuration suitable for hopping. Overlap between the metal 3d and oxygen 2p orbitals along the hopping path highly depends on the bond length and angle, dictating the nature of the transfer process.[4] The figure is reprinted from reference 4.

In the past many years, many experimental techniques have been developed to detect the presence of polarons in materials, including but not limited to scanning tunnelling microscopy and spectroscopy (STM and STS, respectively),[5] angle-resolved photoemission spectroscopy (ARPES),[6] electron paramagnetic resonance (EPR),[7] Raman scattering.[8] In the meantime, the implementation of many-polaron theory has allowed the more precise calculation of polaron-related properties, which includes but not limited to quantum Monte Carlo,[9] first-principles density functional theory (DFT),[10] dynamical mean-field theory (DMFT).[11]

The carrier mobility in hematite is achieved via the hopping of electron polaron, which can be described by the Marcus theory.[12] There are two kinds of hopping mechanisms: adiabatic and diabatic hopping. In the adiabatic hopping scheme, polarons move much faster than the phonon field, therefore, their propagation is much smaller than that of lattice distortions and polarons hop via tunneling from site to site. In contrary, for diabatic hopping scheme, polarons move much slower than the lattice

polarization, hence, the activation energy and prefactor can be calculated by directly employing first-principles schemes defining specific polaron transfer pathways within nudged elastic band methods or linear interpolation schemes.[13,14]

1.2 Applications of Hematite

Due of the advantages such as low cost, high abundance, and good stability, hematite has been an attractive material for many different energy storage and conversion applications. Here we would like to focus on photoelectrochemical (PEC) water splitting and supercapacitors.

1.2.1 PEC Water Splitting

Sunlight is so far the most plentiful renewable energy source (~1.2×10^{14} kJ are received at the Earth's surface every second),[15] however, its intermittent characteristic makes it necessary to convert it to other forms of energy so that the energy can be stored and utilized during night or cloudy days. Hydrogen is an ideal candidate for storing the solar energies because (1) hydrogen is a very clean energy and the combustion product is only water, no environmental pollution and carbon emissions. (2) hydrogen has the largest gravimetric density among all known substances.

PEC water splitting is a great approach to utilize sunlight to split water into hydrogen and oxygen under applied external bias.[16] The oxygen evolution reaction happens on the anode while the hydrogen evolution reaction happens on the cathode. Hematite has been widely used as photoanode material for PEC because its bandgap

around 2.2 eV makes it able to absorb part of the visible light and ultraviolet light (wavelength < 560 nm).[17] Theoretically it was predicted that hematite is able to achieve a solar-to-hydrogen efficiency of 12.9%.[18] However, a real measured solar-to-energy efficiency is much lower compared to the predicted value due to (1) a very short excited state lifetime (~ 1 ps)[19,20] and (2) a small hole diffusion length (~2 to 4 nm).[21] In addition, the conducting band of hematite lies below the H_2 evolution potential, which makes it necessary to apply an external bias for hydrogen generation at the cathode.

Nanostructure engineering and atomic doping are two promising approaches to tackle the aforementioned issues.[17] Smaller size of particle can decrease the diffusion length of carriers to suppress the recombination between electron and holes. For example, Fu *et al.* systematically studied the change of relaxation time for hematite with different particle sizes between 4 nm and 10 nm with pump-probe laser spectroscopy. They found that the smaller hematite particles have longer relaxation time constants compared to larger particles.[22] On the other hand, atomic doping is widely used to increase the excited state lifetime. Wang *et al.* found that after hematite is doped by Ti, the absorption decay profile had a slightly higher amplitude than that of the undoped sample and is indicative of reduced electron–hole recombination on the time scale measured.[23] Another limitation of using hematite as photoanode for PEC measurement is the low electrical conductivity, which will be discussed in detail later.

1.2.2 Supercapacitor

Hematite is also a pseudo-capacitance material, which makes it a candidate for supercapacitors applications, given its large theoretical capacitance. However, the real

capacitive performance of hematite-based device is far from ideal limited by two factors: (1) poor electrical conductivities and (2) sluggish ion transport in the oxide lattice. The electrical conductivities of hematite will be discussed in detail in part 1.3 and structural engineering are commonly used to tackle the sluggish ion transport issue. For example, Liu *et al.* developed an electrochemical approach to synthesize binder-free ultrathin hematite nanoflakes (NFs). Due to the large surface area of NFs, the charge transfer resistance of NF is decreased significantly, and the ion transport is substantially improved. As a result, the ultrathin hematite NFs increased capacitance for about 10-fold and exhibited a better rate capability.[24] Song *et al.* took different approaches to tackle the ion transport problem. They prepared thick hematite films with engineerable mesopore size through a glucose-assisted hydrothermal method. A mesopore size of 3 nm gives the best performance because they not only expose the interior surface of thick films to electrolyte and hence boost ion-accessible surface area, but also serve as reservoirs to improve electrolyte infiltration and reduce ion diffusion length. The engineered hematite films exhibit an areal capacitance of 1502 mF/cm^2 at 1 mA/cm^2, which is one of the top reported capacitance performances of hematite-based device.[25]

1.3 Electrical Conductivities of Hematite

Hematite is an antiferromagnetic material, which means that the spin direction of Fe in adjacent Fe bilayer is alternating while the spin directions of all Fe in the same

Fe bilayer are the same. This strong anisotropic property makes the electron polaron hopping along a-b plane much easier compared to that along c-axis in hematite. It was experimentally measured that the diffusion coefficient of electron transport along a-b plane in hematite is about 3-4 orders higher than that along c-axis.[26] The small polaron hopping mechanism makes the carrier mobility in hematite really low, about 10^{-3} cm^2 V^{-1} s^{-1},[27] while that of Si, another very insulating material, is ~10^3 cm^2 V^{-1} s^{-1}.[28] If we could improve the carrier conductivity of hematite, it is significant since it can improve the performance of many hematite-based devices.

As we all know, the electrical conductivity (σ) in semiconductor can be calculated by using the following equation:

$$\sigma = en\mu \qquad (1.1)$$

where e is the electron charge, n is the carrier concentration and μ is the carrier mobility. Based on equation 1.1, there are two possible approaches we can work on to improve the electrical conductivity of hematite: (1) improve the carrier concentration and (2) improve the carrier mobility. The most used approaches to improve the electrical conductivity is by atomic doping. Although many works have already been done to understand the effect of atomic doping. There are still many questions not well answered yet in the field. For example, how different defects interact with each other when doping concentration keeps on increasing? How do doping change the carrier concentration in hematite and what dopants are the best at raising electron polaron concentration in hematite? How do doping impact the carrier mobility in hematite and

what dopants are the best in improving the carrier mobility in hematite. Only taking traditional experimental approaches is hard to fully answer these questions since it could be very time consuming to test all different possible dopants at different synthesis conditions with different concentrations. In addition, it is difficult to probe into the structural details of different systems. Fortunately, these drawbacks can be addressed by coupling first-principles density functional theory with experimental approaches.

1.4 Density Functional Theory (DFT)

DFT has become a popular method to investigate the properties of molecular and solid-state materials because of the following reasons: (1) it is able to deal with many-body problems with a relatively economical computational cost compared to other high-cost theories such as random-phase approximation, Møller–Plesset perturbation theory, the coupled-cluster singles and doubles method, quantum Monte Carlo calculation, etc. (2) Its accuracy has been improved significantly in the past several decades by using better functionals to a level that is sufficient to explain or predict the properties of interested materials. (3) As shown in Fig. 1, the computational capability worldwide in the past 30 years has an exponential increase, which makes it possible to use DFT to calculate larger and more complicated systems. Due to these advantages, I combined first-principles DFT calculations with experimental approaches together to understand how doping impacts the electrical conductivities of hematite. Some commonly used exchange and correlation functionals will be

introduced below to help readers understand why different functionals can achieve different levels of accuracy.[29]

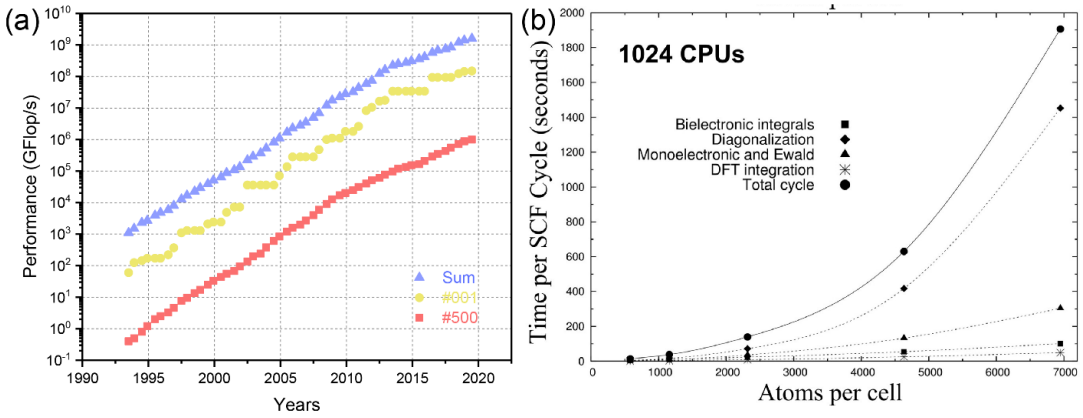

Figure 1.2 Computational capability development and computation time scale with the number of atoms per cell. (a) The y-axis (flop per s) in (a) indicates floating point operations per second, which is a metric to evaluate the computer performance. "#001" means the fastest supercomputer in the world, "#500" means the 500th fastest supercomputer in the world and "Sum" means the summation computational capability of the top 500 supercomputers. (b) Wall-clock time (in seconds) of a SCF cycle run in parallel over 1024 processors for MCM-41 supercells of increasing size with the hybrid B3LYP functional. The time required by the main computational tasks in each SCF cycle is also separately reported.

1.4.1 Local Density Approximation

Local density approximation (LDA) is a class of approximations of the exchange-correlation (XC) energy functional in DFT,[30]

$$E_{XC}^{LDA}[n] = \int \varepsilon_{XC}(n)n(r)d^3r \quad (1.2)$$

among which $E_{XC}^{LDA}[n]$ is the XC energy, $\varepsilon_{XC}(n)$ is the XC energy per particle of a homogeneous electron gas (HEG) of charge density $n(r)$. The XC energy can be decomposed into exchange part (ε_X) and the correlation part (ε_C) linearly,

$$\varepsilon_{XC} = \varepsilon_X + \varepsilon_C \quad (1.3)$$

The ε_X can be calculated from HEG while the ε_C is much harder to get, leading to numerous different approximations for ε_C. Since LDA functional assumes that the electron density is the same everywhere, it tends to underestimate the exchange energy and overestimate the correlation energy. Although it is not a very accurate functional to calculate the XC energy, it is often used to construct more sophisticated XC functional, such as generalized gradient approximation and hybrid functional discussed below.

1.4.2 Generalized Gradient Approximation

To correct the error in LDA, instead of assuming that the electron density is the same everywhere, the gradient of the density is incorporated in the equation to account for the non-homogeneity of the true electron density, the new functional is called generalized gradient approximation (GGA).[31] This allows for corrections based on the changes of density away from the coordinate, which has the following form:

$$E_{XC}^{GGA}[n] = \int \varepsilon_{XC}(n)n(r)d^3r \quad (1.4)$$

among which $E_{XC}^{GGA}[n]$ is the XC energy, $\varepsilon_{XC}(n)$ is the new XC energy particle after taking the gradient of electron density $n(r)$ into consideration. By using GGA, the

calculated molecular geometries and ground-state energies can match better with experimental values.

1.4.3 Hubbard U Corrections

It is well known that LDA and GGA are not accurate enough to correctly describe the Coulomb interaction between 3d electrons localized on metallic ion, and insulating materials are often miscalculated as metallic, or the bandgap is underestimated. In order to solve this problem, Hubbard U is introduced to correctly simulate the Coulomb interaction between 3d electrons localized on metallic ions.[32] For example, if Hubbard U correction is applied to LDA, then we have the following equation:

$$E_{LDA+U}[n] = E_{LDA}[n] + E_U[n_i] - E_{dc}[n_i] \quad (1.5)$$

where $E_U[n_i]$ is the Hubbard U correction, and $E_{dc}[n_i]$ is the "double-counting" term. Because we have added the Hubbard correction explicitly, the energy contribution of these orbitals included in the LDA functional have to be removed to avoid their repeated contributions.

1.4.4 Hartree-Fock method and hybrid approximation

Since the exchange part in previous LDA and GGA method is still estimated, a more accurate method of incorporating a portion of exact exchange from Hartree-Fock theory with the rest of the exchange-correlation energy from other sources is created called hybrid functional.[33] A hybrid exchange–correlation functional is usually constructed as a linear combination of the Hartree–Fock exact exchange functional,

expressed by the following equation, and any number of exchange and correlation explicit density functionals.

$$E_X^{HF} = -\frac{1}{2}\sum_{i,j}\iint \psi_i^*(r_1)\psi_j^*(r_2)\frac{1}{r_{12}}\psi_j(r_1)\psi_i(r_2)dr_1dr_2 \qquad (1.6)$$

Acknowledgements

Y. P. acknowledges the support of the National Science Foundation under Grants No. DMR-1760260 and No. CHE-1904547. Y. L. acknowledges the financial support from the Merced nAnomaterials Center for Energy and Sensing (MACES), a NASA funded MIRO center, under award NNX15AQ01.

References

[1] K. Sivula, F. L. Formal, and M. Grätzel, Chem. Mater. **21,** 2862 (2009).

[2] A. G. Tamirat, J. Rick, A. A. Dubale, W.-N. Su, and B.-J. Hwang, Nanoscale Horiz. **1,** 243 (2016).

[3] C. Franchini, M. Reticcioli, M. Setvin, and U. Diebold, Nat. Rev. Mater. **6,** 560 (2021).

[4] Y. Natanzon, A. Azulay, and Y. Amouyal, Isr. J. Chem. **60,** 768 (2020).

[5] M. Setvin, C. Franchini, X. Hao, M. Schmid, A. Janotti, M. Kaltak, C. G. Van de Walle, G. Kresse, and U. Diebold, Phys. Rev. Lett. **113,** 086402 (2014).

[6] S. Moser, L. Moreschini, J. Jaćimović, O. S. Barišić, H. Berger, A. Magrez, Y. J. Chang, K. S. Kim, A. Bostwick, E. Rotenberg, Phys. Rev. Lett. **110,** 196403 (2013).

[7] C. Di Valentin, G. Pacchioni, A. Selloni, S. Livraghi, and E. Giamello, J. Phys. Chem. B **109,** 11414 (2005).

[8] H. Rho, C. S. Snow, S. L. Cooper, Z. Fisk, A. Comment, and J. P. Ansermet, Phys. Rev. Lett. **88,** 127401 (2002).

[9] N. V. Prokof'ev and B. V. Svistunov, Phys. Rev. Lett. **81,** 2514 (1998).

[10] F. Wu and Y. Ping, J. Mater. Chem. A **6,** 20025 (2018).

[11] S. Fratini and S. Ciuchi, Phys. Rev. Lett. **91,** 256403 (2003).

[12] R. A. Marcus, Rev. Mod. Phys. **65,** 599 (1993).

[13] N. A. Deskins and M. Dupuis, Phys. Rev. B **75,** 195212 (2007).

[14] C. Spreafico and J. VandeVondele, Phys. Chem. Chem. Phys. **16,** 26144 (2014).

[15] N. Armaroli and V. Balzani, Chem. Eur. J. **22,** 32 (2016).

[16] I. Roger, M. A. Shipman, and M. D. Symes, Nat. Rev. Chem. **1,** 0003 (2017).

[17] D. A. Wheeler, G. Wang, Y. Ling, Y. Li, and J. Z. Zhang, Energy Environ. Sci. **5,** 6682 (2012).

[18] A. B. Murphy, P. R. F. Barnes, L. K. Randeniya, I. C. Plumb, I. E. Grey, M. D. Horne, and J. A. Glasscock, Int. J. Hydrogen Energy **31,** 1999 (2006).

[19] A. G. Joly, J. R. Williams, S. A. Chambers, G. Xiong, W. P. Hess, and D. M. Laman, J. Appl. Phys. **99,** 053521 (2006).

[20] U. Bjoerksten, J. Moser, and M. Graetzel, Chem. Mater. **6,** 858 (1994).

[21] J. H. Kennedy and K. W. Frese, J. Electrochem. Soc. **125,** 709 (1978).

[22] L. Fu, Z. Wu, X. Ai, J. Zhang, Y. Nie, S. Xie, G. Yang, and B. Zou, J. Chem. Phys. **120,** 3406 (2004).

[23] G. Wang, Y. Ling, D. A. Wheeler, K. E. N. George, K. Horsley, C. Heske, J. Z. Zhang, and Y. Li, Nano Lett. **11,** 3503 (2011).

[24] T. Liu, Y. Ling, Y. Yang, L. Finn, E. Collazo, T. Zhai, Y. Tong, and Y. Li, Nano Energy **12,** 169 (2015).

[25] Y. Song, T. Liu, M. Li, B. Yao, T. Kou, D. Feng, F. Wang, Y. Tong, X.-X. Liu, and Y. Li, Adv. Energy Mater. **8,** 1801784 (2018).

[26] N. Iordanova, M. Dupuis, and K. M. Rosso, J. Chem. Phys. **122,** 144305 (2005).

[27] K. M. Rosso, D. M. A. Smith, and M. Dupuis, J. Chem. Phys. **118,** 6455 (2003).

[28] P. Norton, T. Braggins, and H. Levinstein, Phys. Rev. B **8,** 5632 (1973).

[29] M. Chen, T. J. Smart, S. Wang, T. Kou, D. Lin, Y. Ping, and Y. Li, J. Mater. Chem. A **8,** 8783 (2020).

[30] D. C. Langreth and M. J. Mehl, Phys. Rev. B **28,** 1809 (1983).

[31] J. P. Perdew, K. Burke, and M. Ernzerhof, Phys. Rev. Lett. **77,** 3865 (1996).

[32] S. L. Dudarev, G. A. Botton, S. Y. Savrasov, C. J. Humphreys, and A. P. Sutton, Phys. Rev. B **57,** 1505 (1998).

[33] D. R. Hartree and W. Hartree, Proc. R. Soc. A: Math. Phys. Eng. Sci. **150,** 9 (1935).

Chapter 2 – The Critical Role of Synthesis Conditions on Small Polaron Carrier Concentrations in Hematite—A First-principles Study

Abstract

Achieving highly efficient energy conversion with transition metal oxides necessitates overcoming conductivity limitations due to the formation of small polarons. Detailed understanding of the interplay among intrinsic defects, dopants, and electron polarons can help devise strategies for achieving higher carrier concentrations, therefore improving carrier conductivity. This work employs first-principles calculations to reliably predict electron polaron concentrations in a prominent polaronic oxide, hematite (Fe_2O_3), by resolving interactions between charged defects and electron polarons and keeping charge neutrality condition among all charged species. This work addresses that both V_O and Fe_i can be primary donors in undoped hematite depending on the synthesis conditions, such as synthesis temperature and oxygen partial pressure, despite the fact that V_O owns an extremely high ionization energy compared to k_BT. Furthermore, from calculations of a plethora of n-type dopants (group IV and V elements), we find that Ti, Ge, Sb, and Nb are able to raise electron polaron concentrations in hematite significantly without considering dopant clustering. However, the magnitude of electron polaron concentration increase would be smaller if the dopant has a high tendency of clustering, such as Ti. We reveal the critical role of synthesis conditions on tuning electron polaron concentrations of both undoped and

doped hematite. Our theoretical analysis provides important insights and general design principles for engineering more conductive polaronic oxides.

2.1 Introduction

Hematite (α-Fe_2O_3) is a promising material for several important applications, such as photoelectrochemical (PEC) water splitting, energy conversion and storage,[1-3] receiving greater attention due to its high abundance, remarkable stability, non-toxicity, and moderate bandgap.[4,5] However, its intrinsic low carrier concentration (primarily small electron polarons in hematite) has created a major bottleneck, which limits the usage of hematite for these applications.[6-8] The most common strategy to overcome this limitation is by atomic doping wherein the substituted dopant may generate electron polarons and enhance electron polaron concentrations, thereby improving efficiency.[8-13]

Yet, outstanding questions remain in the pursuit of highly efficient Fe_2O_3-based devices with atomic doping. For example, the identity of the intrinsic electron polaron donor in undoped hematite remains under debate. Specifically, various experimental works have claimed that oxygen vacancies (V_O) are the source of extra electron polarons in n-type Fe_2O_3,[14] whereas theoretical works have shown that V_O have an extremely large ionization energy compared to k_BT,[15] which suggests that they are not supposed to be the primary contributor of electron polarons. Meanwhile, some other theoretical works have supported that iron interstitials (Fe_i) are the major electron polaron donors due to a significantly smaller ionization energy than that of V_O.[16] Another important question, which is more general to oxides than particularly to Fe_2O_3, is how to determine dopants which will yield the highest carrier concentration? Insights

into the design of efficient oxide-based devices by simple yet practical prediction of atomic doping are highly desired.[2]

There have been several theoretical studies on intrinsic defects and atomic doping in Fe_2O_3; for example, defect formation energy and charge transition levels have been computed for Fe_2O_3, which can help discover dopants with low ionization energy, such as Sn, Ge, and Ti.[15,17] However, these works cannot yet address the above questions since direct evaluation of electron polaron concentrations requires knowledge of the combined effects of dopant solubility and ionization energy from all intrinsic defects and extrinsic dopants in the system at the charge neutrality condition. Intrinsic defects should be considered simultaneously as they may compensate the electrons or holes from dopants, and yet, the effects of intrinsic defects with or without external doping are not well-established in Fe_2O_3 so far, as mentioned above.

In this work, we answer these questions by calculating electron polaron concentrations in Fe_2O_3 under various conditions from first-principles. By careful evaluation of defect concentrations in the presence of small electron polarons, we can reliably predict the concentrations of electron polarons in Fe_2O_3, in excellent agreement with experiments at similar conditions. Further detailed computational analysis of dopant solubility, ionization energy, chemical condition, and synthesis temperature is provided in order to answer outstanding questions. What are the intrinsic major electron polaron donors in undoped Fe_2O_3? Which dopants are the best at raising electron polaron concentrations? What makes a dopant effective in raising electron polaron concentrations (e.g., high solubility or low ionization energy)? The work is organized

as follows. First, we discuss intrinsic defects in undoped Fe_2O_3. Second, we systematically study tetravalent and pentavalent dopants, identifying the best dopants for this system. Third, we analyze the importance of solubility against ionization energy in enhancing electron polaron concentrations in hematite as a function of synthesis conditions. Fourth, we reveal the general trends of formation energy/ionization energy within each group with respect to ionic radius. Finally, we investigate the effect of dopant clustering on electron polaron concentration. The contribution of entropy to the formation free energy is also rigorously considered. This work provides an in-depth and comprehensive study of the interactions among intrinsic defects, extrinsic dopants, and small polarons and their effects on carrier concentrations in polaronic oxides.

2.2 Methodologies

2.2.1 First-principles Calculations

Density functional theory (DFT) calculations were performed in the open-source plane-wave code QuantumESPRESSO[18] using ultrasoft GBRV pseudopotentials[19] and an effective Hubbard U[20] value of 4.3 eV for Fe 3d orbitals.[15,21] Plane-wave cutoff energies of 40 and 240 Ry were used for wavefunctions and charge density, respectively. For all calculations except phonon frequency ones, we employed a $2 \times 2 \times 2$ supercell (120 atoms) of the hexagonal unit cell with a $2 \times 2 \times 2$ k-point mesh for the integration over the Brillouin zone.

2.2.2 Elemental Chemical Potentials

The chemical potentials of Fe and O were evaluated from first-principles following the approach employed in previous paper.[16] Particularly, for Fe_2O_3 in thermodynamic equilibrium growth conditions, the chemical potentials μ_{Fe} and μ_O must satisfy equations (2.1)–(2.3),

$$2\mu_{Fe} + 3\mu_O = E_{Fe_2O_3} \quad (2.1)$$

$$2\mu_O \leq E_{O_2} \quad (2.2)$$

$$3\mu_{Fe} + 4\mu_O \leq E_{Fe_3O_4} \quad (2.3)$$

In an O rich environment, Fe_2O_3 will be in equilibrium with O_2 as in equation (2.2), whereas in an O poor environment (Fe rich), Fe_2O_3 will be in equilibrium with Fe_3O_4 as in equation (2.3). In order to correct the well-known overbinding problem of O_2 by DFT, we used the experimental value of 5.23 eV for the binding energy of O_2.[22] Meanwhile, the chemical potential of each dopant X was computed as in previous paper.[17] Specifically, the chemical potentials of dopants μ_X are limited by

$$\mu_X + 2\mu_O \leq E_{XO_2} \quad (2.4)$$

$$2\mu_X + 5\mu_O \leq E_{Fe_2O_3} \quad (2.5)$$

to avoid formation of secondary phases between dopants and oxygen [equation (2.4) for group IV elements and equation (2.5) for group V elements]. After obtaining the chemical potential of O in the rich/poor limit, we will obtain the corresponding dopant chemical potentials through equations (2.4) and (2.5). The chemical potentials of

dopant X are also restricted by their elemental solids: $\mu_X \leq E_X$. In order to show the effect of oxygen partial pressure on defect and electron polaron concentrations, we relate chemical potential of oxygen to oxygen partial pressure at finite temperature.

2.2.3 Charged Defect Formation Energy and Concentration

Charged defect formation energies and defect concentrations, including carrier concentrations, were evaluated from first-principles. Note that unless specified, defects include both intrinsic defects and extrinsic dopants in this work. First, the formation energies for each defect (X) at a charge state q were obtained according to

$$E_q^f(X;\varepsilon_F) = E_q(X) - E_{prist} + \sum_i \mu_i \Delta N_i + q\varepsilon_F + \Delta_q \qquad (2.6)$$

where $E_q(X)$ is the total energy of the defect system (X) with charge q, E_{prist} is the total energy of the pristine system, μ_i and ΔN_i are the elemental chemical potential and change in the number of atomic species i, and ε_F is the Fermi energy. A charged defect correction Δ_q to remove spurious interactions of a charged defect with its periodic images and background counter-charge was computed with techniques developed before as implemented in the JDFTx code.[23-25] The elemental chemical potentials were carefully evaluated against the stability of by-product compounds as detailly discussed in 2.2.2. The corresponding charge transition levels (CTLs) of the defects were obtained from the value of ε_F where the stable charge state transitions from q to q',

$$\varepsilon_{q|q'} = \frac{E_q^f(X) - E_{q'}^f(X)}{q' - q} \qquad (2.7)$$

The ionization energies are computed by referencing the CTLs to the free polaron state. Specifically, in Fe_2O_3,[26-29] it has been experimentally observed that photoexcited carriers relax on the picosecond timescale to form small polarons,[7] which have been measured to form at energies 0.5 eV below the conduction band minimum (CBM).[6,8] Theoretically, this free polaron level is computed as the charge transition level from q = 0 to q = -1 in the pristine system, $\varepsilon_{FP} = \varepsilon_{-1|0}^{prist} = E_{-1}^{f}(prist) - E_{0}^{f}(prist)$. By this method, we obtain that the free polaron level is positioned at 0.497 eV below the CBM in excellent agreement with experimental observation.[6,8] By referencing to this state instead of the CBM, ionization energy defined in equation (2.7) reflects the energy that it takes to form a free polaron for conduction from a defect-bound polaron. The CTLs of all surveyed dopants in this work are listed in Fig 2.1. Finally, charged defect concentration (c_q) can be computed directly from the charged defect formation energies,

$$c_q(X;\varepsilon_F) = g exp\left[-E_q^f(X;\varepsilon_F)/k_B T\right] \quad (2.8)$$

where g is the degeneracy factor accounting for the internal degrees of freedom of the point defect, k_B is the Boltzmann factor, and T is the temperature. Two temperatures are introduced during the evaluation of defect concentrations. First, a synthesis temperature (T_S) simulating an experimental synthesis condition is employed to determine the concentration of each defect at different charge states, satisfying the charge neutrality condition, which is expressed as

$$\sum_{q,X} q c_q(X) + n_h + n_e = 0 \quad (2.9)$$

where n_h and n_e are free delocalized hole and electron concentrations. Second, while keeping the concentration of each defect (sum of all charge states) the same as that at synthesis temperature, charge neutrality condition is reinforced at operating temperature (T_O: room temperature in this work). This procedure will change the relative concentration of different charge states for a defect at T_O (although defect concentrations with summing up all charge states are kept unchanged as the ones at T_S), with the ratio between different charge states as[16]

$$\frac{c_q(X;\varepsilon_F)}{c_{q'}(X;\varepsilon_F)} = \frac{exp\left[-E_q^f(X;\varepsilon_F)/k_BT\right]}{exp\left[-E_{q'}^f(X;\varepsilon_F)/k_BT\right]} \tag{2.10}$$

By evaluating charge neutrality, the defect concentrations can be uniquely determined at a particular oxygen partial pressure and synthesis temperature without external parameters.

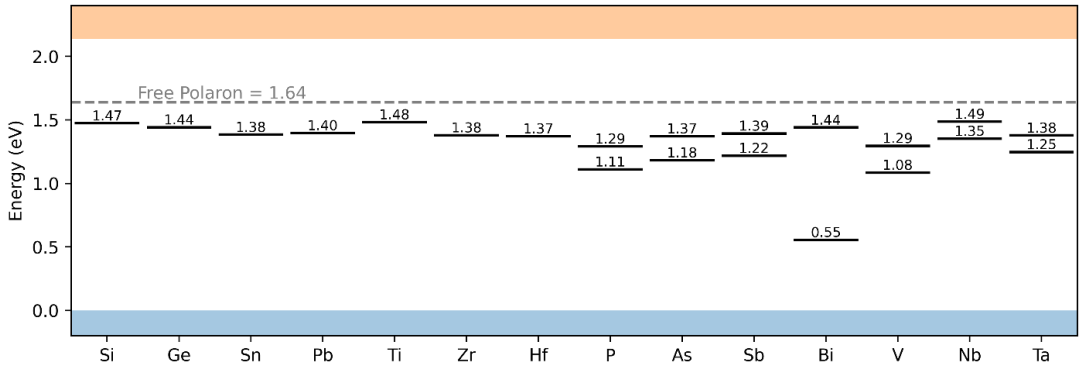

Figure 2.1 Charge transition levels of all different dopants considered in this study. For group IV dopants, the short solid black line is corresponding to 0/+1 charge transition level, while for group V dopants, the upper short solid black line is for 0/+1 and the lower short solid black line is for +1/+2 charge transition level.

2.2.4 Entropy

The effect of entropy is also rigorously considered in this work, which includes two parts: configurational entropy and vibrational entropy. The configurational entropy is computed based on the assumption of an ideal solution (reasonable at the dilute doping limit),[30,31] while vibrational entropy is calculated with first-principles phonon frequencies and an entropy expression as detailed in the supplementary material. We compute phonon frequencies of 60 atom hexagonal supercells at the Γ-point by using density functional perturbation theory at the DFT+U level as implemented in the Vienna Ab initio Simulation Package (VASP).[32-34]

2.3 Small Polarons and Intrinsic Defect Concentrations in Undoped Hematite

The intrinsic source of electron carriers in undoped Fe_2O_3 has been the subject of debate for a long time. Here, the electron carriers include both free small electron polarons and free delocalized electrons in principles; however, the latter has negligible concentrations in Fe_2O_3. In undoped hematite, intrinsic defects, such as vacancies (V_O, V_{Fe}) and interstitials (O_i, Fe_i), may form within the lattice along with the generation of carriers, mainly small electron polarons (EPs). Their formation energy plots at different conditions (O rich, one atmosphere, and O poor environment) are shown in Fig. 2.2. Since V_O and Fe_i are n-type defects, they introduce small electron polarons into the

lattice with the corresponding EP wavefunctions shown in Figs. 2.3(a) and 2.3(b). In Fig. 2.3(c), intrinsic defect concentrations (including vacancies and interstitials) are provided at room temperature (300 K) as a function of oxygen partial pressure (p_{O_2}) in undoped hematite for three synthesis temperatures (T_S = 873, 1073, and 1373 K, corresponding to 600, 800, and 1100 ^oC commonly used in experiment). First, we note that the defect with the highest concentration is V_O (sum of all charged states of oxygen vacancies, lowest formation energy in Table I), which should be chiefly responsible for the nonstoichiometry observed in Fe_2O_3.[35] Second, we find that intrinsically excess electrons can form into free electron polarons [dashed red line labeled as EP in Fig. 2.3(c)], whereas the concentrations of free delocalized electrons and holes are negligible (less than 10^8 cm^{-3}), consistent with experimental measurements showing EPs being the majority of photoexcited electrons in Fe_2O_3.[7] Also, the lower formation energy of V_O and Fe_i compared with p-type defects (V_{Fe} and O_i) in Table 2.1 is consistent with the intrinsic n-type nature of Fe_2O_3.

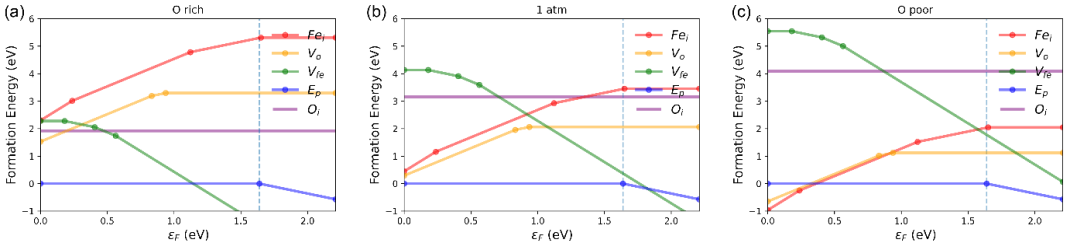

Figure 2.2 Formation energy of tetravalent dopants (left) and pentavalent dopants (right) computed at p_{O_2} = 1 atm. The dashed line represents the free electron polaron energy, which is used as the reference energy instead of CBM for the ionization energy of n-type dopants in Fe_2O_3.

In terms of identifying the primary donor of these EPs, the conclusions are dependent on the synthesis conditions and cannot be determined from formation energy or ionization energies alone. At T_S = 873 K, it is the case that ionized oxygen vacancies [V_O^+, dashed purple line in Fig. 2.3(c)] are the primary donor to free electron polaron concentrations (overlaps with the dashed red line labeled as EP). Interestingly, as the synthesis temperature is elevated, for example, to T_S = 1373 K, free electron polaron concentrations are not just more abundant; they are also generated from a different source, i.e., Fe interstitials [Fe_i^+, solid light blue line in Fig. 2.3(c)]. The switch of the primary donor to electron polarons and their concentrations as a function of synthesis temperature are shown in Fig. 2.3(d) (at p_{O_2} = 1 atm). We find that for synthesis temperatures below a critical temperature of 1104 K, V_O^+ is the primary donor, whereas above this threshold, Fe_i^+ will become the primary donor. To simultaneously show the effect of oxygen partial pressure, we plot heat maps of electron polaron concentrations and the difference between Fe_i^+ and V_O^+ concentrations in Figs. 2.3(e) and 2.3(f). The close resemblance between the two figures reveals the importance of forming Fe_i in achieving higher electron polaron concentrations in undoped Fe_2O_3. Our results suggest that previous debate over the primary donor in pristine hematite can be explained by the transition from V_O^+ to Fe_i^+ while increasing synthesis temperature, which has not been identified before. Furthermore, this transition highlights the varying importance of defect solubility vs ionization energy. While the ionization energy of V_O is as high as 0.7 eV, it has the highest solubility among intrinsic defects (Table 2.1). At lower

synthesis temperatures (e.g., below 1100 K), the formation of Fei is sparse [less than 10^{10} cm^{-3} at T_S = 873 K as shown in Fig. 2.3(c)], and by consequence, V_O is the primary source of electron polarons. In this situation, the electron polaron concentrations are extremely low, 10^{12} cm^{-3}, because the Fermi level is pinned at the first charge transition level of V_O at 0.7 eV below the free electron polaron level. This observation is in good agreement with recent measurements of undoped Fe_2O_3, which exhibit Fermi level positions between 0.8 and 1.2 eV referenced to CBM.[8] When the synthesis temperature is increased or the oxygen partial pressure is decreased, the formation of Fe_i is more achievable and eventually, it can act as the major electron polaron donor in Fe_2O_3. In this situation, Fe_i is always ionized to Fe_i^+ due to a negative ionization energy, -0.01 eV, and therefore, the electron polaron concentrations of hematite can be dramatically increased [blue regions in Figs. 2.3(d)–2.3(f) where Fe_i^+ is the primary donor, and EP concentrations can reach 10^{18} cm^{-3}]. In this situation, the Fermi level will approach the free polaron limit as experimentally observed.[8]

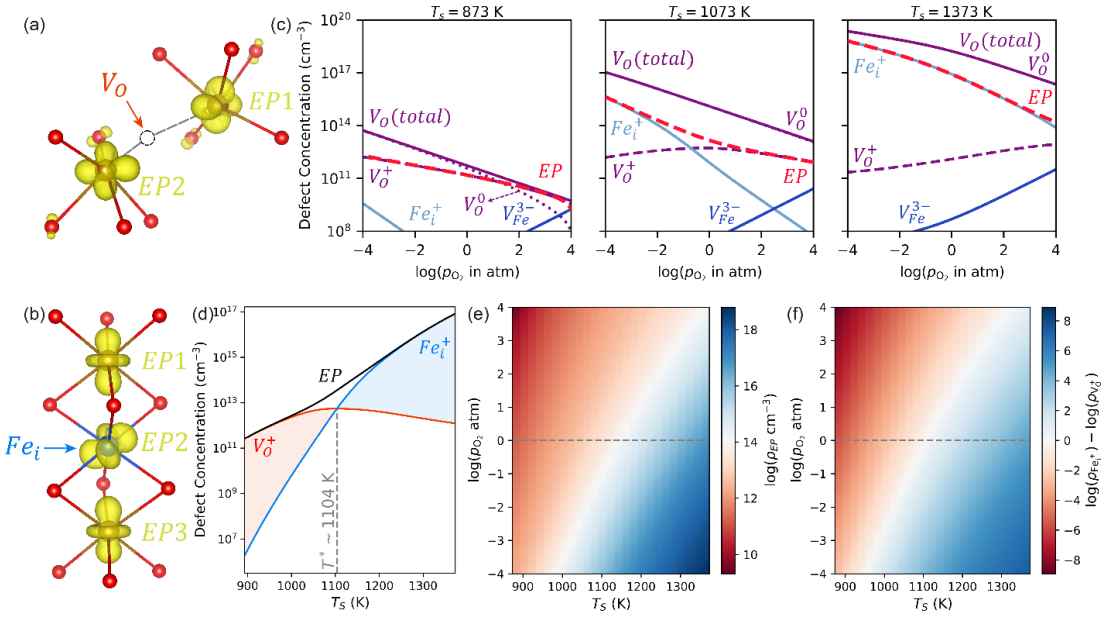

Figure 2.3 Identification of the source of a major electron polaron donor in undoped Fe_2O_3. (a) Local structure and electron wavefunctions (yellow cloud) of V_O with two EPs. (b) Local structure and electron wavefunctions of Fei with three EPs (one of which forms at the Fe interstitial site). (c) Intrinsic defect concentrations as a function of oxygen partial pressure in undoped hematite computed at room temperature equilibrium conditions with different synthesis temperatures (T_S) at T_S = 873, 1073, and 1373 K. (d) V_O^+, Fe_i^+ and EP concentrations at room temperature and p_{O_2} = 1 atm as a function of T_S. (e) Free electron polaron concentration (ρ_{EP}) and (f) the difference between Fe_i^+ and V_O^+ ($\rho_{Fe_i^+} - \rho_{V_O^+}$) at the room temperature operating condition as a function of synthesis temperature (T_S) and oxygen partial pressure (p_{O_2}). In the atomic plots, gold = Fe, red = O, and blue = Fe_i. The yellow cloud is an isosurface of the polaron wavefunction with an isosurface level of 1% of its maximum.

Table 2.1 The formation energy (E_f) at the neutral state and ionization energies (electron affinities) of intrinsic defects at p_{O_2} = 1 atm in undoped Fe_2O_3, where IE represents ionization energy and EA is electron affinity. IE references to a free electron polaron level, while EA references to VBM.

Defect	E_f (eV)	***IE*** **(0/+1) (eV)**	***IE*** **(+1/+2) (eV)**	***IE*** **(+2/+3) (eV)**	***EA*** **(-1/0) (eV)**	***EA*** **(-2/-1) (eV)**	***EA*** **(-3/-2) (eV)**
V_O	2.06	0.70	0.81	--	--	--	--
Fe_i	3.46	-0.01	0.52	1.40	--	--	--
V_{Fe}	4.14	--	--	--	0.18	0.41	0.56
O_i	3.15	--	--	--	--	--	--

2.4 Small Polarons and Defect Concentrations in Doped Hematite

In order to achieve higher electron polaron concentrations and optimize the efficiency of Fe_2O_3-based devices, extrinsic doping will be necessary. Here, we broadly investigate potential dopants and identify optimal doping strategies by considering all group IV and V elements as substitutional dopants. Intuitively substituting trivalent Fe ions by tetravalent or pentavalent ions will donate electrons due to the increased valence electron count. In Fig. 2.4, we only show the atomic structures and electronic structures of two representative extrinsic dopants (Ti and Nb) that we find enhancing

electron polaron concentration of Fe_2O_3 significantly, under typical synthesis conditions, e.g., p_{O_2} = 1 atm and T_S = 1073 K.[36] Since the two electron polarons of an Nb dopant (group V) could occupy different Fe sites, different possible configurations are rigorously considered to find the most stable one [Fig. 2.4(d)]. Although the energy levels of the two electron polaron states are very close to each other, they are actually not degenerate [Figs. 2.4(e) and 2.4(f)]. Our predictions of Ti, Ge, Sb, Nb, and Sn as effective dopants in raising elecron polaron concentrations to 10^{19}–10^{20} cm^{-3} are consistent with experimental measurements as well (Table 2.2). The excellent agreement with experiments on various dopants highlights the robustness of our first-principles prediction of equilibrium dopant and carrier concentrations. An important note from our calculations is that although group V in principles can provide two free electrons from each dopant, we did not see that they are guaranteed to give larger electron polaron concentrations compared to group IV dopants as shown in Table 2.2. The reason is that the second ionization energy of group V elements can be much larger and difficult to contribute to electron polaron concentrations.

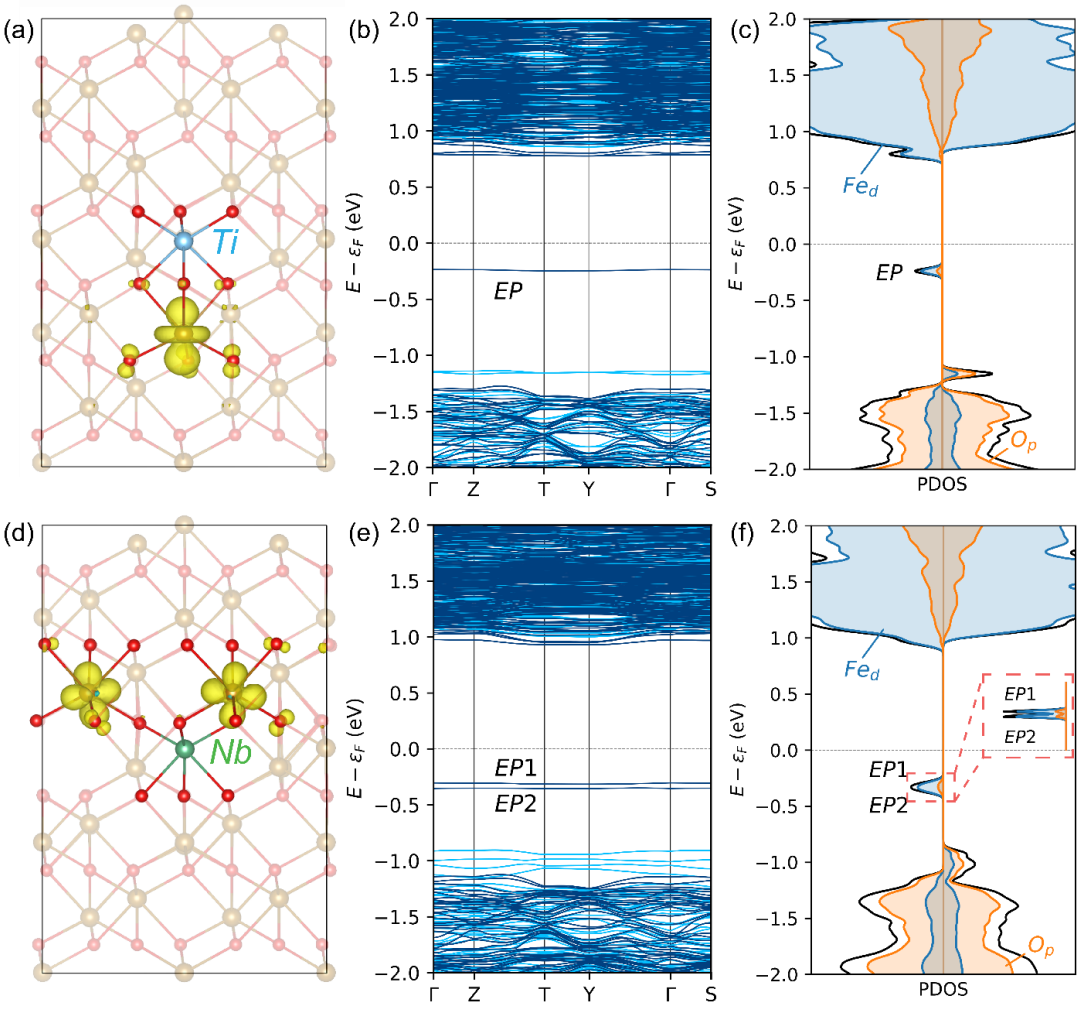

Figure 2.4 Atomic structures and electronic structures of two representative extrinsic dopants, which raise electron polaron concentrations in Fe_2O_3 significantly. (a) Atomic structure, (b) band structure, and (c) projected density of states (PDOS) of Fe_2O_3 doped with Ti. (d) Atomic structure, (e) band structure, and (f) PDOS of Fe_2O_3 doped with Nb. Here gold = Fe, red = O, and the remaining-colored atom is the dopant as labeled within each figure. The yellow cloud is an isosurface of the polaron wavefunction with an isosurface level of 1% of its maximum.

Table 2.2. Summary of the four representative dopants with their formation energy at the neutral state ($\boldsymbol{E_f}$) at p_{O_2} = 1 atm, first ionization energy [$\boldsymbol{IE}$ (0/+1)], second ionization energy [$\boldsymbol{IE}$ (+1/+2)], electron polaron concentration (ρ_{EP}, computed at room temperature with synthesis at 873, 1073, 1373 K, and p_{O_2}= 1 atm), and corresponding experimentally measured electron polaron concentrations. Both IE reference to a free electron polaron level as before.

Dopant	**Si**	**P**	**Nb**	**Ti (no clustering)**	**Ti (clustered)**
E_f (eV)	1.949	1.926	1.461	0.884	1.535
IE (0/+1) (eV)	0.165	0.348	0.153	0.157	0.308
IE (+1/+2) (eV)	--	0.528	0.287	--	0.361
ρ_{EP} (cm^{-3}) (T_S: 873K)	1.35×10^{15}	6.57×10^{15}	2.04×10^{18}	1.39×10^{19}	1.34×10^{19}
ρ_{EP} (cm^{-3}) at T_S: 1073K	1.4×10^{17}	1.8×10^{17}	2.2×10^{19}	7.4×10^{19}	3.5×10^{19}
ρ_{EP} (cm^{-3}) at T_S: 1373K	7.24×10^{18}	1.19×10^{18}	1.54×10^{20}	2.80×10^{20}	2.04×10^{20}
ρ_{EP}^{exp} (cm^{-3})	--	--	~10^{19}[37]	10^{19}-10^{20} [38-44]	10^{19}-10^{20} [38-44]

Table 2.3. Collected ionic radius (R_I, valency 4+ or 5+, coordination VI),[45] single dopant formation energy (E_f, computed for a neutral dopant at p_{O_2} = 1 atm), first ionization energy (IE(0/+1)), second ionization energy (IE(+1/+2)), and free electron polaron concentration (ρ_{EP}, computed at room temperature with synthesis at T_S = 1073K and p_{O_2}= 1 atm) and corresponding experimentally measured electron polaron concentrations for each dopant. Note: both IEs are referenced to free polaron level.

Dopant	R_I **(pm)**	E_f **(eV)**	**IE (0/+1) (eV)**	**IE (+1/+2) (eV)**	ρ_{EP} **(cm^{-3})**	ρ_{EP}^{exp} **(cm^{-3})**
Ti	60.5	0.884	0.157		7.4×10^{19}	$10^{19} - 10^{20}$
Ge	53	0.810	0.197		4.7×10^{19}	$\sim 10^{19}$
Sb	60	0.546	0.247	0.422	4.1×10^{19}	$\sim 10^{20}$
Nb	64	1.461	0.153	0.287	2.2×10^{19}	$\sim 10^{19}$
Bi	76	1.155	0.198	1.084	1.4×10^{19}	
As	46	0.808	0.268	0.456	1.3×10^{19}	
Sn	69	0.883	0.255		1.2×10^{19}	$10^{18} - 10^{20}$
Pb	77.5	1.061	0.241		9.0×10^{18}	
Ta	64	1.224	0.260	0.391	6.1×10^{18}	
Hf	71	1.143	0.267		4.2×10^{18}	
Zr	72	1.230	0.259		3.7×10^{18}	
V	54	1.137	0.344	0.554	1.0×10^{18}	
P	38	1.926	0.348	0.528	1.8×10^{17}	
Si	40	1.949	0.165		1.4×10^{17}	

2.5 Effects of Synthesis Conditions on Polaron and Defect Concentrations

Next, we study the effect of synthesis conditions (synthesis temperature and oxygen partial pressure) on polaron and defect concentrations in extrinsically doped hematite. These two factors affect polaron and defect concentrations via different mechanisms. For example, the decrease of oxygen partial pressure lowers oxygen chemical potentials, which increases the dopants' chemical potentials [set by Eqs. (4) or (5)] and lowers their formation energy. As a result, the dopant concentration and the polaron concentration can be increased. On the other hand, polaron and dopant concentrations can be tuned by the synthesis temperature through the Boltzmann distribution. We pick four dopants (Ti, Si, Nb, and P) as examples (Fig. 2.5). It is clear that some dopants raise electron polaron concentrations more than other dopants, for example, Ti over Si and Nb over P (Fig. 2.5). A natural question is raised: what is the most important factor for a dopant or an intrinsic defect to increase electron polaron concentrations, e.g., low formation energy or low ionization energy?

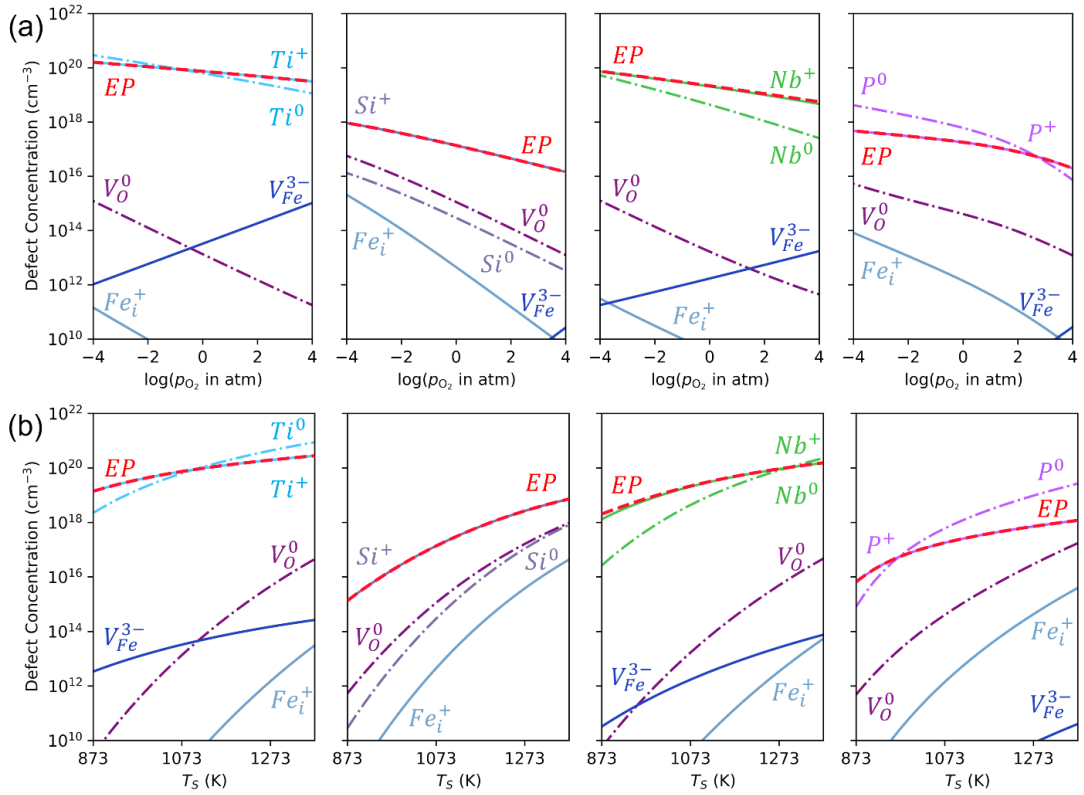

Figure 2.5 The changes of polaron and defect concentrations in doped hematite with respect to synthesis conditions (oxygen partial pressure and synthesis temperature). Room temperature intrinsic defects, dopants, and electron polaron concentrations of Ti, Si, Nb, and P doped hematite at (a) T_S = 1073 K as a function of p_{O_2} partial pressure and (b) p_{O_2} = 1 atm as a function of synthesis temperature T_S.

In order to directly answer this question, we performed a linear regression on the larger data sets obtained from dopant calculations to analyze the importance of dopant formation energy or solubility against that of ionization energy to contributing to electron polaron concentrations at different synthesis temperatures. Fig. 2.6(b) shows the predictive score (e.g., the coefficient of determination R^2) of modeling electron polaron concentration over either formation energy (blue line) or ionization energy (red line) or both (black line) at different synthesis temperatures. Fig. 2.6(c)–2.6(e) give the fitting of electron polaron concentrations over dopant formation energies at three synthesis temperatures (873, 1073, and 1373 K). For example, at T_S = 873 K [Fig. 2.6(c)], the R^2 of a fitting electron polaron concentration over the formation energy corresponds to the first data point in blue line in Fig. 2.6(b), while the data points in red line correspond to R^2 of fitting over ionization energy (not shown). When fitting with both dopant formation energies and ionization energies (black), the predictive score typically exceeds 0.85, which signifies that these two properties fully determine the electron polaron concentrations since intrinsic defect contribution to electron polaron concentrations is negligible in comparison as shown in Fig. 2.5. We note that the deviation of the predictive score from 1 could be due to ignoring the second ionization energy of group V dopants in the fitting in Fig. 2.6(b).

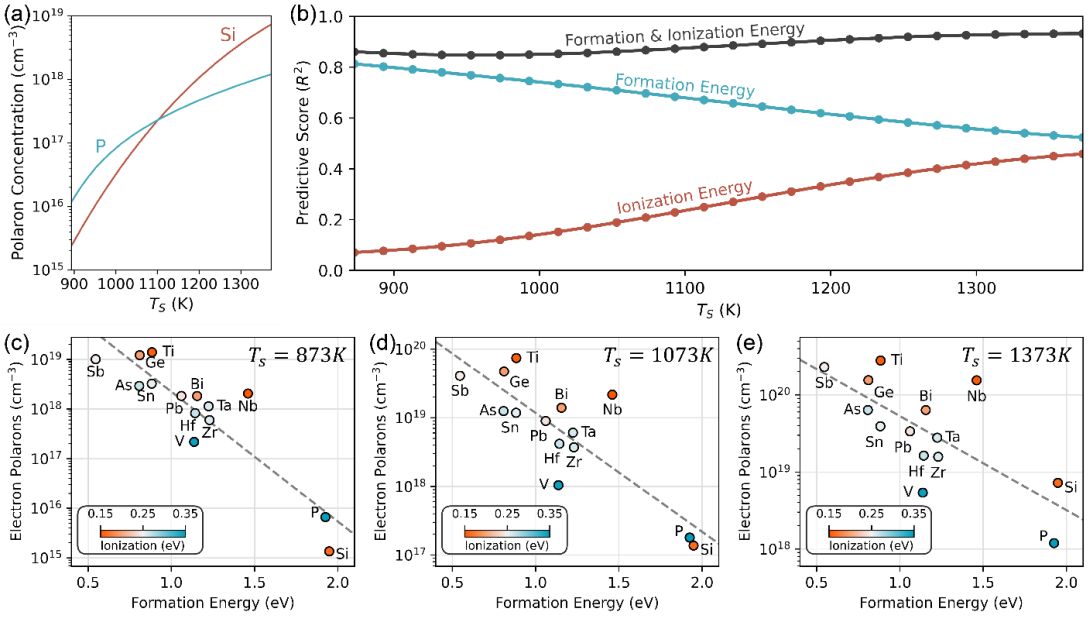

Figure 2.6 Resolving the importance of dopant formation energy and ionization energy in determining electron polaron concentrations of Fe_2O_3. (a) Electron polaron concentration change of Si (red) and P (blue) doped hematite at room temperature and $p_{O_2} = 1$ atm as a function of synthesis temperature (T_S). (b) Predictive score of linear regression models on the induced electron polaron concentrations using dopant formation energy (blue), dopant ionization energy (red), or both (black). Electron polaron concentrations at room temperature and $p_{O_2} = 1$ atm for various synthesis temperatures: (c) 873, (d) 1073, and (e) 1373 K, plotted against dopant formation energies and with dopant ionization energies distinguished in colors.

For lower temperatures, the solubility of the dopant (formation energy, $R^2 \sim 0.8$) almost determines how well the dopant is able to raise electron polaron concentrations,

while ionization energy is significantly less important (R^2 ~ 0.1). This explains why V_O, despite a significantly larger ionization energy (0.7 eV) than Fe_i (-0.01 eV), is still the major donor in undoped Fe_2O_3 at lower synthesis temperatures due to much lower formation energy of V_O 2.06 eV vs Fe_i 3.46 eV (Table 2.1). This can also explain the observation in Table 2.2 and Fig. 2.6(a) that Si underperforms P at low synthesis temperature (T_S = 873 K) due to its slightly higher formation energy (Si: 1.946 eV vs P: 1.926 eV), despite a significant difference in their ionization energy (Si: 0.165 eV and P: 0.348). As the synthesis temperature is elevated, poor solubility can be overcome, and dopants' ability to be ionized is weighted equally [blue and red lines approach R^2 ~ 0.5 in Fig. 2.6(b)]. This explains the dramatic increase in the polaron concentration under Si doping by increasing the synthesis temperature shown in Fig. 2.6(a), as well as the transition from V_O to Fe_i above T_S = 1104 K as the primary electron donor in undoped Fe_2O_3 shown in Figs. 2.3(c)–1(f). Additionally, we conclude that less soluble dopants, such as Si, require a higher synthesis temperature to reach its optimal electron polaron concentrations compared to more soluble dopants, such as Ti, Ge, and Sb (Table 2.2).

On the other hand, we also analyze the importance of dopant formation energy/ionization energy to electron polaron concentrations as a function of oxygen partial pressure (Fig. 2.7), among which formation energy is always more dominant than ionization energy across the entire oxygen partial pressure range. This is expected since the oxygen partial pressure affects the dopants' formation energy through its

relation to the dopants' elemental chemical potential but does not correlate with ionization energy directly.

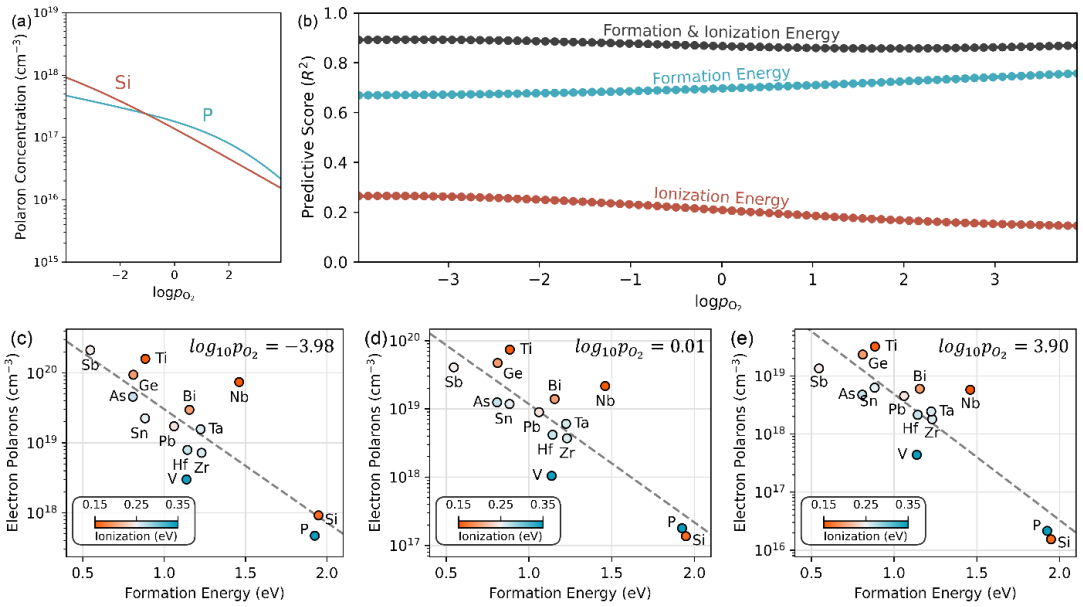

Figure 2.7 Resolving the importance of dopant formation energy and ionization energy in determining electron polaron concentrations of Fe_2O_3. (a) Electron polaron concentration change of Si (red) and P (light green) doped hematite at room temperature and T_S =1073K as a function of oxygen partial pressure. (b) Predictive score of linear regression models on the induced electron polaron concentrations using dopant formation energy (light green), dopant ionization energy (red), or both (black). Electron polaron concentrations at room temperature and T_S = 1073K for various oxygen partial pressure (atm): (c) $log_{10}O_2 = -3.98$, (d) $log_{10}O_2 = 0.01$, and (e) $log_{10}O_2 = 3.90$, plotted against dopant formation energies and with dopant ionization energies distinguished in colors.

2.6 Trends Between Formation Energy/Ionization Energy and Ionic Radius

Moreover, some elemental-specific trends between the formation energy/ionization energy and the ionic radius of dopants within each group are observed. The formation energies of dopants in each group have a parabolic shape with respect to their ionic radius [Fig. 2.8(a)]. Some dopants, such as Ti and Sb, have small formation energies (high solubility), while some others, such as P and Pb, have much higher formation energies (lower solubility). A radius around 60 pm seems to correspond to the minimum formation energy, which is smaller than the ionic radius of Fe^{3+} (64.5 pm). The reason is that the formation of a small electron polaron expands the crystal lattice locally; therefore, a smaller ionic radius of dopants is desired to mitigate the expansion strain from electron polarons. On the other hand, in Fig. 2.8(b), the trends of ionization energies as a function of ionic radius for group IV and group V elements are different. For group V elements, ionization energies generally get smaller with increasing ionic radius (blue and green dots). However, the trend is opposite for group IV elements (red and orange dots). Specifically, ionization energies generally increase with ionic radius. These trends could provide useful guidance to experimentalists on what dopants to choose based on simple known constants, such as an elemental ionic radius.

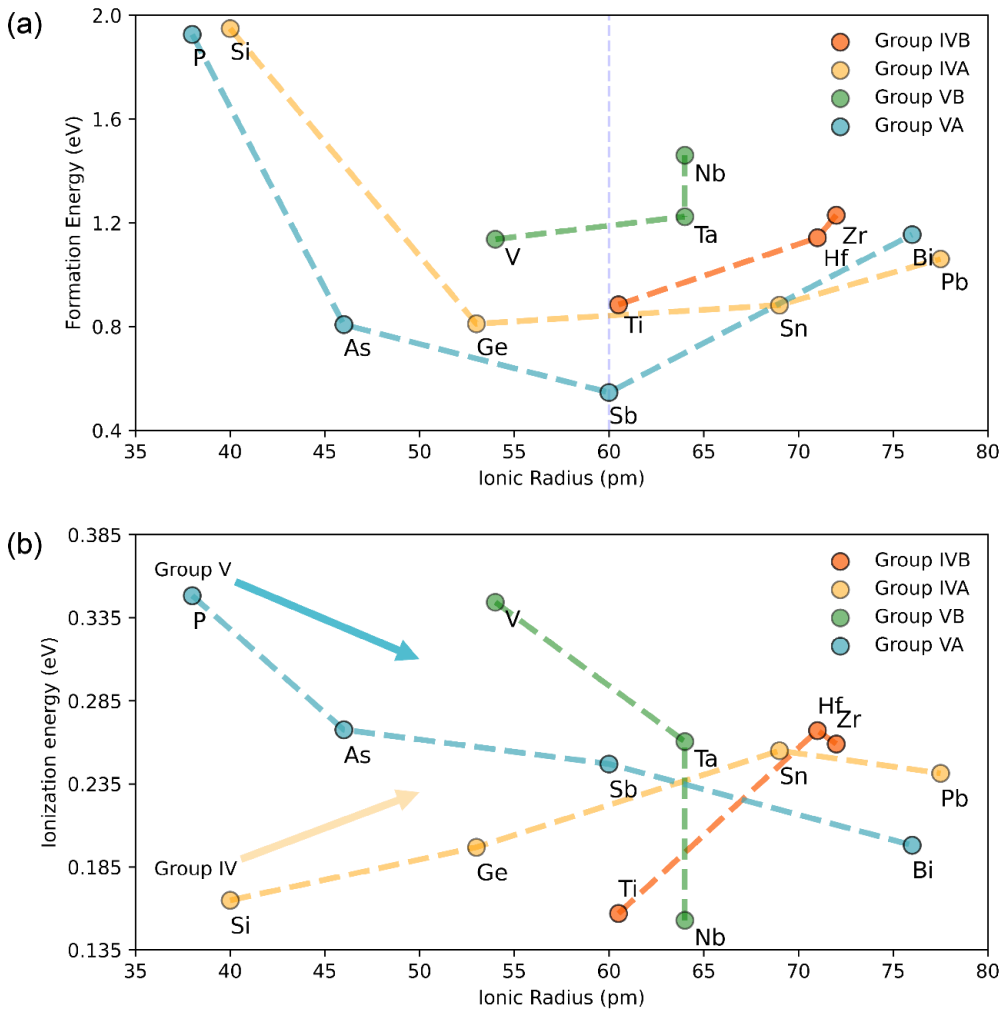

Figure 2.8 Trends of dopant formation energies/ionization energies with respect to the ionic radius in each group of elements. (a) The correlation between formation energies and ionic radius of dopants in each group. (b) The correlation between ionization energies and the ionic radius of dopants in each group.

2.7 Effects of Clustering on Polaron Concentrations

In this section, we discuss the consequence of dopant clustering by forming electric multipoles in hematite, recently shown to be responsible for the doping bottleneck of hematite.[46] Dopant clustering at various synthesis temperatures and partial pressures was calculated using the method described in our previous work.[46] We found that clustering binding energy and formation energy of dopants together determine how much dopant clustering affects the EP concentration. We picked three representative dopants, Ti, Si, and P, as examples to discuss the effect of clustering to EP (Fig. 2.9). Owing to the very negative quadrupole binding energy (-0.23 eV) of Ti, clustering significantly decreases EP concentration and a maximum emerges, as opposed to the concentration that simply increases with the synthesis temperature. The EP_c concentration is contributed both from ionized non-clustered Ti (Ti_{nc}^{+}) and ionized clustered Ti (Ti_{c}^{+}). Besides Ti, Ge is the only other element we found that dopant clustering has non-negligible effects on polaron concentration. On the other hand, although Si is also a group IV element and has a very negative clustering binding energy (-0.23 eV), the EP concentration changes little in response to the clustering effect. The reason behind this is the high formation energy of Si clusters (3.67 eV), which results in a low concentration of Si clusters, therefore, barely changes EP concentrations. Group V elements also have inconsequential clustering effects but for a different reason. They were found to have very large positive binding energies (> 10 eV), indicating that these elements do not favor cluster formation in hematite. Unlike electric multipole formation with group IV elements, group V elements with two

donated electrons cannot form such stable multipoles; therefore, we do not need to consider a similar type of dopant clustering with group V elements. P is also plotted in Fig. 2.9 as a representative case for group V elements. Since most dopants' EP concentration is not significantly affected by dopant clustering, our previous conclusions are unchanged.

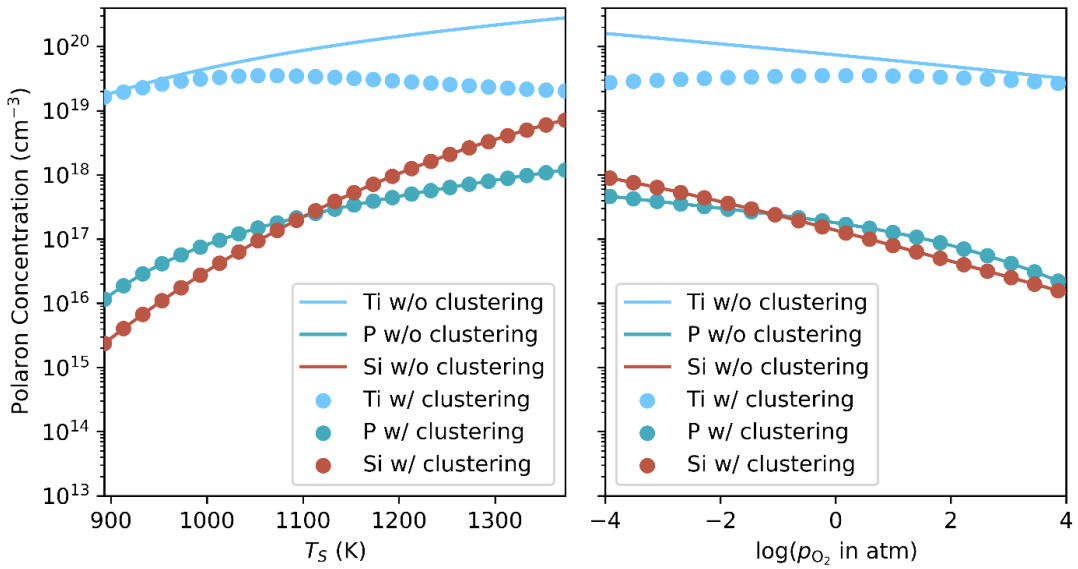

Figure. 2.9 The effects of dopant clustering to the EP concentration at different synthesis temperatures and oxygen partial pressures. Room temperature dopants (Ti, Si, and P) and electron polaron concentrations at (left panel) p_{O_2} = 1 atm as a function of synthesis temperature T_S and (right panel) T_S = 1073 K as a function of p_{O_2}.

2.8 Entropy

At last, we carefully examined the effect of entropy at finite temperature on the formation free energy, as well as polaron and defect concentrations. Entropy contributes to formation free energy from two aspects: configurational entropy and vibrational entropy. Configurational entropy depends on the number of different possible configurations for the defect to be placed in a hematite lattice, which always stabilizes the dopant formation (lower formation free energy). It can again be separated into two parts, configurational entropy from an ideal solution, in which all constituent atoms are treated equal in size and randomly placed in space and excess entropy taking into account of the atomic size difference, the atomic packing fraction, and the number of elements. Since the latter part is much smaller than the former for defects at the dilute limit, in this work, the configurational entropy of an ideal solution is used to approximate the total configurational entropy. On the other hand, the vibrational entropy is computed for each system entering formation energy definition in equation (2.6).[47,48] We choose Sn and Nb as two representatives for group IV and V elements and find their entropy contribution to the formation free energy to be 0.1–0.2 eV (Fig. 2.10 and 2.11), which does not affect polaron and defect concentrations significantly. Therefore, formation energy without entropy contributions is mostly used in this work unless specified since calculating entropy for all dopants is computationally intensive.

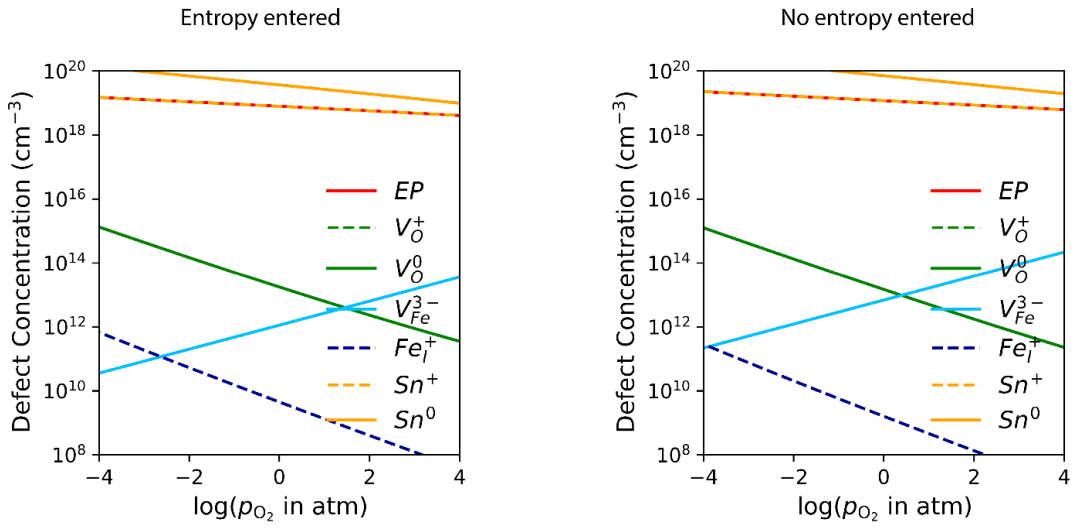

Figure 2.10 Defect and electron polaron concentrations in Sn doped hematite (a) with entropy and (b) without entropy entering the formation free energy computed at room temperature as operation temperature with synthesis at T_S = 1073K.

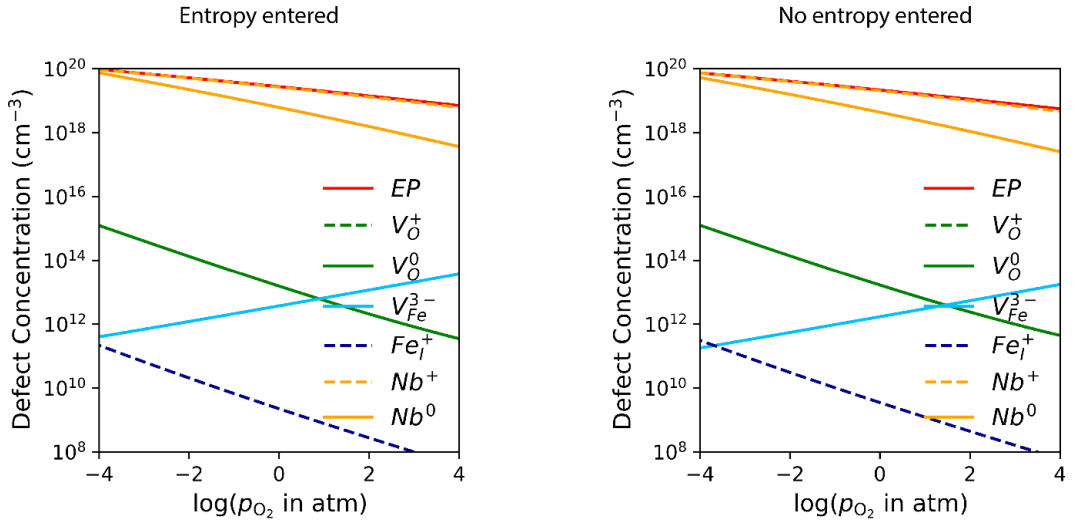

Figure 2.11 Defect and electron polaron concentrations in Nb doped hematite (a) with entropy and (b) without entropy entering the formation free energy computed at room temperature as operation temperature with synthesis at T_S = 1073K.

2.9 Conclusion

In summary, this work demonstrates the interplay among intrinsic defects, dopants, and small polarons in determining carrier concentrations in a prototypical oxide, Fe_2O_3. This work identifies the critical role of synthesis conditions, such as synthesis temperature and oxygen partial pressure on carrier concentrations (primarily small electron polarons) in hematite, both undoped and doped, from first-principles calculations. For undoped hematite, the major electron donor switches from V_O to Fe_i with ramping up synthesis temperature. For doped hematite, the increase of synthesis temperature or lowering of oxygen partial pressure both can increase the electron polaron concentration. However, the increased magnitude is affected by clustering with a form of electric multipoles. For example, without considering the effect of clustering, Ti is the best dopant in boosting electron polaron concentrations among all dopants we surveyed. Nonetheless, the high tendency of clustering for Ti dramatically lowers the electron polaron concentration, while for other dopants, such as Si and group V elements, which have low tendency of such clustering, it has negligible effects on electron polaron concentrations. Although formation energy is more dominant in determining EP concentrations than ionization energy in hematite for most cases, tuning synthesis conditions, such as increasing synthesis temperature, could overcome the poor solubility issue of certain dopants, which suggests that less soluble dopants, such as Si, will require elevated synthesis temperatures to boost EP concentrations. Quenching would be one possible approach to mitigate the clustering of dopants such as Ti and Ge. This work answers several outstanding questions for hematite, which are

also applicable to other polaronic oxides. Therefore, our work deepens the fundamental understanding on tuning carrier concentration and provides important guidelines for material design and synthesis, required by efficient energy conversion and storage devices.

Acknowledgements

This work was supported by the National Science Foundation (NSF) under Grant Nos. DMR-2003563 and CHE-1904547. Part of this work was performed under the auspices of the U.S. Department of Energy (DOE) by the Lawrence Livermore National Laboratory under Contract No. DE-AC52-07NA27344. T.J.S. acknowledges the LLNL Graduate Research Scholar Program and funding support from LLNL LDRD 20-SI-004. This research used resources of the Scientific Data and Computing center, a component of the Computational Science Initiative, at the Brookhaven National Laboratory under Contract No. DE-SC0012704; the lux supercomputer at UC Santa Cruz, funded by the NSF MRI grant (No. AST 1828315); the National Energy Research Scientific Computing Center (NERSC), a U.S. Department of Energy Office of Science User Facility operated under Contract No.DE-AC02-05CH11231; and the Extreme Science and Engineering Discovery Environment (XSEDE), which is supported by the NSF (Grant No. ACI-1548562).[49]

Reference

[1] I. Roger, M. A. Shipman, and M. D. Symes, Nat. Rev. Chem. **1,** 0003 (2017).

[2] Y. Yang, S. Niu, D. Han, T. Liu, G. Wang, and Y. Li, Adv. Energy Mater. **7,** 1700555 (2017).

[3] H. Tang, W.-J. Yin, M. A. Matin, H. Wang, T. Deutsch, M. M. Al-Jassim, J. A. Turner, and Y. Yan, J. Appl. Phys. **111,** 073502 (2012).

[4] A. G. Tamirat, J. Rick, A. A. Dubale, W.-N. Su, and B.-J. Hwang, Nanoscale Horiz. **1,** 243 (2016).

[5] T. Jiang, F. Bu, X. Feng, I. Shakir, G. Hao, and Y. Xu, ACS Nano **11,** 5140 (2017).

[6] E. Pastor, J.-S. Park, L. Steier, S. Kim, M. Grätzel, J. R. Durrant, A. Walsh, and A. A. Bakulin, Nat. Commun. **10,** 3962 (2019).

[7] L. M. Carneiro, S. K. Cushing, C. Liu, Y. Su, P. Yang, A. P. Alivisatos, and S. R. Leone, Nat. Mater. **16,** 819 (2017).

[8] C. Lohaus, A. Klein, and W. Jaegermann, Nat. Commun. **9,** 4309 (2018).

[9] A. Rakita, N. Nikolić, M. Mildner, J. Matiasek, and A. Elbe-Bürger, Sci. Rep. **10,** 1 (2020).

[10] M. Li, Y. Yang, Y. Ling, W. Qiu, F. Wang, T. Liu, Y. Song, X. Liu, P. Fang, Y. Tong, Nano Lett. **17,** 2490 (2017).

[11] Y. Yang, M. Forster, Y. Ling, G. Wang, T. Zhai, Y. Tong, A. J. Cowan, and Y. Li, Angew. Chem. Int. Ed. **55,** 3403 (2016).

[12] Y. Ling, G. Wang, D. A. Wheeler, J. Z. Zhang, and Y. Li, Nano Lett. **11,** 2119 (2011).

[13] P. Liao and E. A. Carter, J. Appl. Phys. **112,** 013701 (2012).

[14] M. Kunitski, N. Eicke, P. Huber, J. Köhler, S. Zeller, J. Voigtsberger, N. Schlott, K. Henrichs, H. Sann, F. Trinter, Nat. Commun. **10,** 1 (2019).

[15] T. J. Smart and Y. Ping, J. Phys.: Condens. Matter **29,** 394006 (2017).

[16] J. Lee and S. Han, Phys. Chem. Chem. Phys. **15,** 18906 (2013).

[17] Z. Zhou, P. Huo, L. Guo, and O. V. Prezhdo, J. Phys. Chem. C **119,** 26303 (2015).

[18] P. Giannozzi, S. Baroni, N. Bonini, M. Calandra, R. Car, C. Cavazzoni, D. Ceresoli, G. L. Chiarotti, M. Cococcioni, I. Dabo, J. Phys.: Condens. Matter **21,** 395502 (2009).

[19] K. F. Garrity, J. W. Bennett, K. M. Rabe, and D. Vanderbilt, Comput. Mater. Sci. **81,** 446 (2014).

[20] S. L. Dudarev, G. A. Botton, S. Y. Savrasov, C. J. Humphreys, and A. P. Sutton, Phys. Rev. B **57,** 1505 (1998).

[21] N. Adelstein, J. B. Neaton, M. Asta, and L. C. De Jonghe, Phys. Rev. B **89,** 245115 (2014).

[22] L. Wang, T. Maxisch, and G. Ceder, Phys. Rev. B **73,** 195107 (2006).

[23] R. Sundararaman and Y. Ping, J. Chem. Phys. **146,** 104109 (2017).

[24] F. Wu, A. Galatas, R. Sundararaman, D. Rocca, and Y. Ping, Phys. Rev. Mater. **1,** 071001 (2017).

[25] R. Sundararaman, K. Letchworth-Weaver, K. A. Schwarz, D. Gunceler, Y. Ozhabes, and T. A. Arias, SoftwareX **6,** 278 (2017).

[26] H. Seo, Y. Ping, and G. Galli, Chem. Mater. **30,** 7793 (2018).

[27] A. Radmilovic, T. J. Smart, Y. Ping, and K.-S. Choi, Chem. Mater. **32,** 3262 (2020).

[28] C. Zhou, Z. Sanders-Bellis, T. J. Smart, W. Zhang, L. Zhang, Y. Ping, and M. Liu, Chem. Mater. **32,** 6401 (2020).

[29] D. Lee, V. U. Baltazar, T. J. Smart, Y. Ping, and K.-S. Choi, ACS Appl. Mater. Interfaces **12,** 29275 (2020).

[30] Y. F. Ye, Q. Wang, J. Lu, C. T. Liu, and Y. Yang, Intermetallics **59,** 75 (2015).

[31] Y. F. Ye, Q. Wang, J. Lu, C. T. Liu, and Y. Yang, Mater. Today **19,** 349 (2016).

[32] S. Baroni, S. de Gironcoli, A. Dal Corso, and P. Giannozzi, Rev. Mod. Phys. **73,** 515 (2001).

[33] G. Kresse and J. Furthmüller, Comput. Mater. Sci. **6,** 15 (1996).

[34] G. Kresse and J. Furthmüller, Phys. Rev. B **54,** 11169 (1996).

[35] R. Dieckmann, Philos. Mag. A **68,** 725 (1993).

[36] C. M. Tian, W. W. Li, Y. M. Lin, Z. Z. Yang, L. Wang, Y. G. Du, H. Y. Xiao, L. Qiao, J. Y. Zhang, L. Chen, J. Phys. Chem. C **124,** 12548 (2020).

[37] C. Sanchez, K. D. Sieber, and G. A. Somorjai, J. Electroanal. Chem. Interf. Electrochem. **252,** 269 (1988).

[38] N. T. Hahn and C. B. Mullins, Chem. Mater. **22,** 6474 (2010).

[39] J. A. Glasscock, P. R. F. Barnes, I. C. Plumb, and N. Savvides, J. Phys. Chem. C **111,** 16477 (2007).

[40] M. Rioult, H. Magnan, D. Stanescu, and A. Barbier, J. Phys. Chem. C **118,** 3007 (2014).

[41] K. D. Malviya, D. Klotz, H. Dotan, D. Shlenkevich, A. Tsyganok, H. Mor, and A. Rothschild, J. Phys. Chem. C **121,** 4206 (2017).

[42] G. Wang, Y. Ling, D. A. Wheeler, K. E. N. George, K. Horsley, C. Heske, J. Z. Zhang, and Y. Li, Nano Lett. **11,** 3503 (2011).

[43] O. Zandi, B. M. Klahr, and T. W. Hamann, Energy Environ. Sci. **6,** 634 (2013).

[44] Z. Fu, T. Jiang, Z. Liu, D. Wang, L. Wang, and T. Xie, Electrochim. Acta **129,** 358 (2014).

[45] R. Shannon, Acta Crystallogr. A **32,** 751 (1976).

[46] T. J. Smart, V. U. Baltazar, M. Chen, B. Yao, K. Mayford, F. Bridges, Y. Li, and Y. Ping, Chem. Mater. **33,** 4390 (2021).

[47] T. Kou, M. Chen, F. Wu, T. J. Smart, S. Wang, Y. Wu, Y. Zhang, S. Li, S. Lall, Z. Zhang, Nat. Commun. **11,** 590 (2020).

[48] T. Kou, T. Smart, B. Yao, I. Chen, D. Thota, Y. Ping, and Y. Li, Adv. Energy Mater. **8,** 1703538 (2018).

[49] J. Towns, T. Cockerill, M. Dahan, I. Foster, K. Gaither, A. Grimshaw, V. Hazlewood, S. Lathrop, D. Lifka, G. D. Peterson, Computing in Science & Engineering **16,** 62 (2014).

Chapter 3 – The Impacts of Doping on the Small Polaron Carrier Mobility and Conductivity in Hematite

Abstract

Hematite (α-Fe_2O_3) is a promising transition metal oxide for many different energy conversion and storage applications due to advantages of low cost, high abundance, and good chemical stability. However, its low carrier mobility and electrical conductivity have hindered wide application of hematite-based devices. Fundamentally, this is mostly caused by the formation of small polarons, instead of delocalized carriers, which conduct through thermally activated hopping. Atomic doping is one of the most promising approaches to improve electrical conductivity in hematite. However, its mechanistic impact on carrier mobility and electrical conductivity at the atomistic level remain to be understood. In this work, through a kinetic Monte-Carlo sampling plus statistical average approach, we calculated the carrier concentration and carrier mobility of the doped hematite by taking contributions from individual Fe layers, given its dominant in-plane carrier transport properties. We then studied how different dopants impact carrier mobility in hematite by taking Sn, Ti, and Nb as examples. It was found that the carrier mobility change is related to the disorder of Fe-Fe pair distances, i.e., the more disordered and stretched Fe-Fe pair distances are, the lower carrier mobility will be. Therefore, elements which limit long-range disorder of the Fe sub-lattice are the ideal candidates for improving the carrier mobility in hematite. Our work revealed how dopants impact carrier mobility and

conductivity in hematite and provided practical guidelines to experimentalists on the choice of dopants for optimal electrical conductivity and performance of hematite-based devices.

3.1 Introduction

Hematite is a promising transition metal oxide, and its advantages such as low cost, high abundance, and good chemical stability make it widely used in energy conversion and storage applications. The bandgap around 2.2 eV also makes it an ideal material for light absorption, therefore, it is widely used for photoelectrochemical (PEC) water splitting. Calculations predict that hematite could achieve a theoretical solar-to-hydrogen conversion efficiency of 12.9%.[1] However, the experimentally measured efficiency is far lower than the theoretical one.[2-5] One of the main reasons is the low electrical conductivity of hematite due to the formation of small polarons.[6] The electron polaron (EP) hopping mechanism in hematite requires thermal activation to overcome the energy barrier (greater than 0.1 eV) then achieve carrier transport, which is too high compared to room temperature k_BT (0.0259 eV). Therefore, improving the carrier mobility and electrical conductivity of hematite is essential and highly desired to boost the performance of hematite-based device. Atomic doping is one of the most widely used approaches to improve the low electrical conductivity in hematite. Many experimental and theoretical works have been done to study the effect of atomic doping on the carrier mobility and electrical conductivity of hematite.[7-10] Experimentally, Tian *et al.* synthesized Sn doped hematite and measured the energy barrier of EP hopping. It was found that Sn doping could decrease the energy barrier significantly.[7] Theoretically, Liao *et al.* studied the effect of different group IV dopants on the electron transport in hematite and found that n-type dopants with low ionization energy or stronger covalent interaction with nearby oxygen are beneficial to increase the carrier

concentration while not inhibiting transport.[8] Kerisit *et al.* employed kinetic Monte Carlo model to study the diffusion of EP in hematite and found that attractive defects would slow the EP diffusion due to trapping.[9] Zhou *et al.* used molecular dynamics and revealed that Si doping could improve the mobility of hematite by lowering activation energies and creating low energy EP states.[10]

Although many progresses have been made in the field, many pieces are still missing from the puzzle. First, so far there is no work showing a robust approach to consider both carrier concentration and carrier mobility to compute the electrical conductivity in hematite and comparing that with experimental values. Thanks to our built-in code, we are able to take into account the interplay between different charged defects and correctly evaluate the charge neutrality condition,[11] which gives us carrier concentration matching well with experimental measured ones. In terms of the carrier mobility, the alternating spin direction of Fe bilayers in hematite along c-axis makes EP hopping in this direction not favorable, about 3-4 orders slower than that along a-b plane. Considering the strong anisotropic EP behavior,[12] we choose to neglect the electrical conductivity along c-axis and assemble electrical conductivity in each layer to represent the overall electrical conductivity in the material. Second, how does atomic doping change the carrier mobility degeneracy in different layers? Carrier mobility of different layers in doped hematite depends on its distance from the dopant. Understanding the disruption of doping to the degeneracy of carrier mobility is essential for us to obtain an overall electrical conductivity. Last, what dopants are the best at improving electrical conductivity? What makes them effective in improving

electrical conductivity? The answers to these questions are highly desired since they will provide practical guidance to experimentalists on what dopants to choose to optimize the electrical conductivity in hematite and performance of hematite-based device.

The work is organized as follows. First, the EP hopping in pristine hematite is discussed as reference. For doped hematite, Sn, Nb, and Ti are picked and studied. Different configurations of EP locating at different Fe sites are obtained, followed by Boltzmann distribution, the energy distribution of different configurations is converted to probability distribution, from which the carrier concentration in each layer can be obtained. Second, all possible EP hopping in each layer are computed, and an effective hopping barrier and mobility of each layer is obtained by employing kinetic Monte Carlo (kMC) sampling. The overall electrical conductivity of the whole system can be calculated by summing up the product of carrier concentration and carrier mobility in each layer. In the end, the three dopants are computed in this work to reveal the trend of how different dopants impact the electrical conductivity in hematite. We found that the carrier mobility of hematite will decrease after atomic doping no matter what elements are used since some Fe-Fe pair distances are stretched. The carrier mobility is correlated to the level of disorder in the Fe sub-lattice. The more disordered the Fe-Fe pair distance is, the lower the carrier mobility is. The intuition is that the longer Fe-Fe pair distance is corresponding to the larger energy barrier as indicated by the relative shift of potential energy surface between initial state (IS) and final state (FS). Therefore, dopants with minimal disruption of Fe-Fe sublattices are more suitable in terms of

carrier mobility. This work solves previous unaddressed issues and deepens our understanding of how dopants impact the carrier mobility and electrical conductivity in hematite.

3.2 Methodologies

3.2.1 First-principles Calculations

All energy calculations were performed by employing the plane-wave density functional theory (DFT) code QUANTUM ESPRESSO[13] and an effective Hubbard U[14] value of 4.3 eV is applied for Fe 3d orbitals.[15,16] Plane-wave cutoff of 40 Ry and 240 Ry were used for wavefunction and charge density cutoffs, respectively. Configurations were relaxed with an energy threshold of 10^{-4} Ry/Å using GBRV pseudopotentials.[17] We employed a hexagonal $2 \times 2 \times 1$ supercell with a k-point mesh of $2 \times 2 \times 2$ to integrate over the Brillouin zone. We calculated the EP energy distribution at different Fe sites for both $2 \times 2 \times 1$ supercell and $3 \times 3 \times 1$ supercell and found that the energy difference between the corresponding configuration is smaller than 0.15 eV (Fig. 3.1). Considering the high computational cost for calculating $3 \times 3 \times 1$ supercell and relatively small errors of $2 \times 2 \times 1$ supercell compared to $3 \times 3 \times 1$ supercell, we employed $2 \times 2 \times 1$ supercell for all other calculations in the work.

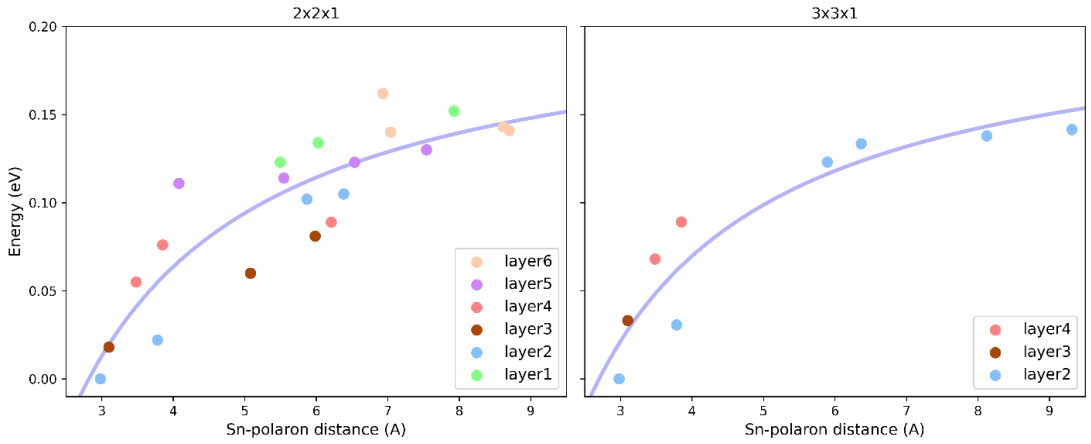

Figure 3.1 The energy distribution of EP locating at different Fe sites as a function of Sn-polaron distance for (a) $2 \times 2 \times 1$ and (b) $3 \times 3 \times 1$ supercells.

3.2.2 Kinetic Monte Carlo Sampling and Effective Energy Barrier

All possible EP hopping in each layer are calculated. Since the degeneracy of different Fe sites is broken after doping, we made a diagram to make it more convenient to refer to different Fe sites (Fig. 3.2). The supercell is divided into different layers and for each layer, the Fe sites are also labeled with different numbers according to the distance of Fe site to the vertical center of supercell. Dopant is always substituting the middle Fe site in layer 3. Fe sites which are closer to the vertical center have smaller label number. All possible EP hopping in Sn, Ti, and Nb doped hematite are calculated and listed in Table 3.1, 3.2, and 3.3, respectively. Some hopping barriers were not able to be calculated due to the inability to stabilize the EP on specific sites and only hopping between nearest neighbor Fe ions were considered. In the Nb doped system there is no layer 6 as polarons were not stable on this layer.

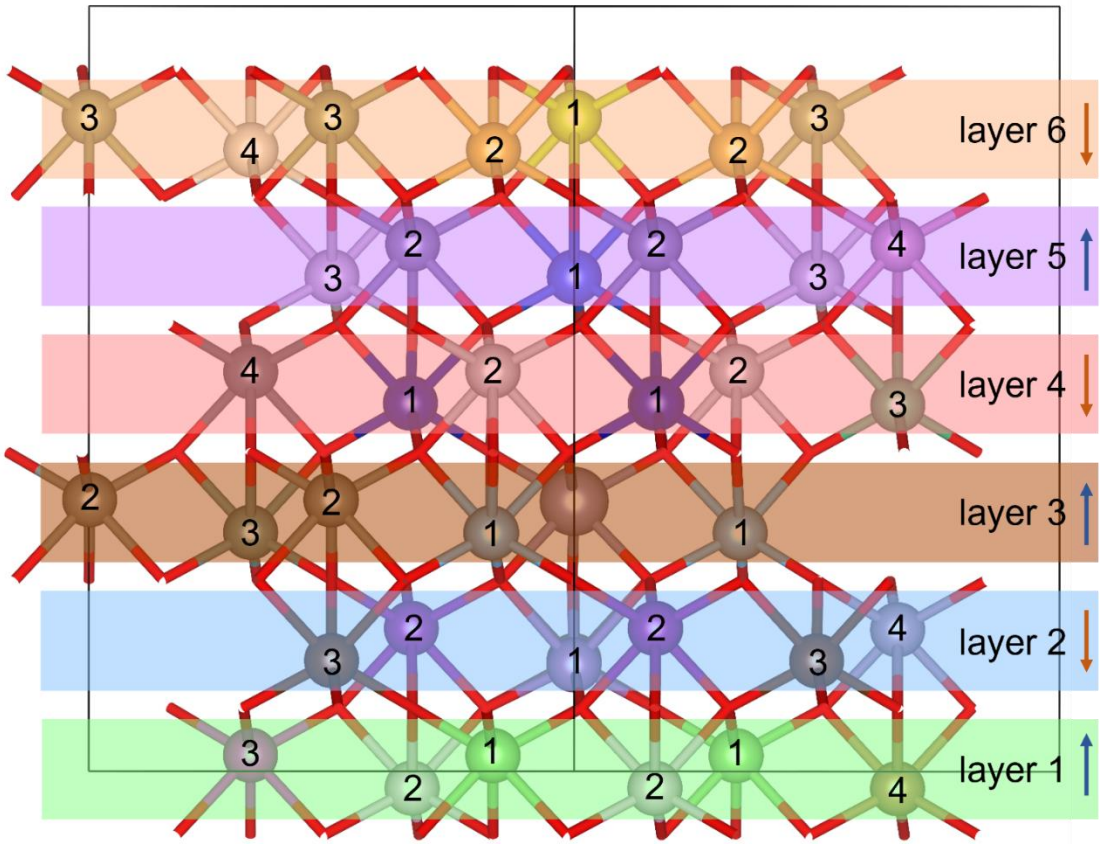

Figure 3.2 The schematic diagram of hematite. Dopant is substituting the middle Fe site in layer 3, as indicated by the different ionic size.

Table 3.1 Details about layers, IS, FS, energy difference between IS and FS ($E_{FS} - E_{IS}$) and energy barrier (E_a) of all possible EP hopping for Sn doped hematite.

Layer	IS	FS	$E_{FS} - E_{IS}$ (eV)	E_a (eV)
1	1	2	0.011	0.142
	1	4	0.029	0.139
2	1	2	0.022	0.160
	2	3	0.080	0.185
	3	4	0.003	0.139
3	1	2	0.043	0.170
	2	3	0.020	0.145
4	1	2	0.022	0.178
	2	3	0.013	0.140
5	1	2	0.003	0.138
	2	3	0.009	0.154
	3	4	0.007	0.140
6	2	1	0.022	0.137
	2	3	0.003	0.139

Table 3.2 Details about layer, IS, FS, energy difference between IS and FS ($E_{FS} - E_{IS}$) and energy barrier (E_a) of all possible EP hopping for Ti doped hematite.

Layer	IS	FS	$E_{FS} - E_{IS}$ (eV)	E_a (eV)
1	1	2	0.003	0.141
	1	4	0.033	0.142
2	1	2	-0.063	0.092
	2	3	0.070	0.187
	3	4	-0.002	0.138
3	1	2	0.026	0.155
	2	3	0.018	0.149
4	1	2	0.045	0.179
	2	3	-0.006	0.130
5	1	2	0.013	0.146
	2	3	-0.014	0.140
	3	4	0.030	0.165
6	1	2	-0.033	0.101
	2	3	0.001	0.135

Table 3.3 Details about layer, IS, FS, energy difference between IS and FS ($E_{FS} - E_{IS}$) and energy barrier (E_a) of all possible EP hopping for Nb doped hematite.

Layer	IS	FS	$E_{FS} - E_{IS}$ (eV)	E_a (eV)
1	1	2	-0.010	0.129
	1	4	0.031	0.139
2	1	2	0.003	0.147
	2	3	0.118	0.210
	3	4	0.000	0.150
3	1	2	0.077	0.200
	2	3	0.038	0.148
4	1	2	0.064	0.223
	2	3	-0.012	0.130
5	1	2	0.022	0.142
	2	3	-0.007	0.150
	3	4	0.040	0.169

All unique in-plane energy barriers were used to setup a kMC calculation to compute the effective energy barrier for each layer in each dopant system. The kMC model was adopted from a previous small polaron mobility simulation in $BiVO_4$.[18] First, the diffusion coefficient is obtained by fitting mean squared displacement (MSD) over time as shown in equation 3.1,

$$D = \lim_{t \to \infty} \frac{<MSD(t)^2>}{2Nt} \quad (3.1)$$

where D is the diffusion coefficient, t is time, N is the number of dimensions, here N is 2 since only diffusion in ab plane is considered. To ensure convergence of the MSD from kMC simulations, each of the MSD was averaged from 16 individual runs with each sampled 12800 times. Convergence is confirmed by comparing with simulation sampled 100 and 1200 times as seen in Fig. 3.2. Second, the same procedures were repeated at various temperature to obtain diffusion coefficients at different temperatures (400, 500, 600, 700, 800, 900, 1000, 1250, and 1500 K). The effective barrier was then determined by fitting the slope of the Arrhenius relation of diffusion coefficients and temperature from equations 3.2,

$$D = D_0 e^{-\frac{E_a}{k_B T}} \quad (3.2)$$

where D_0 is the diffusion pre-factor, E_a is the effective activation, $k_B T$ is thermal energy.

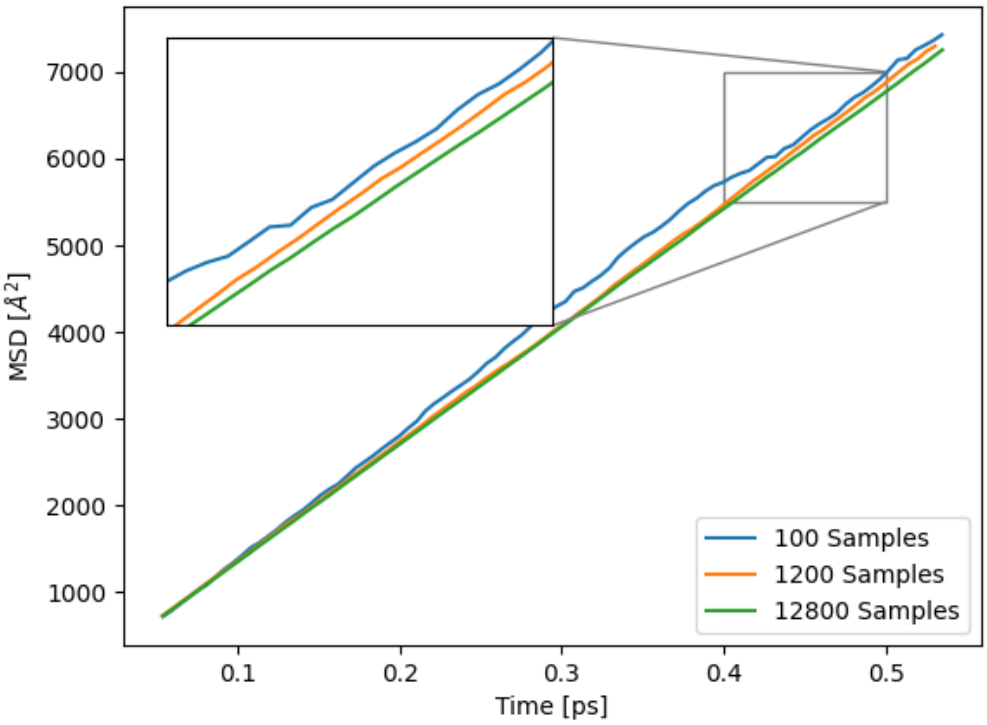

Figure 3.3 MSD over time for kMC simulations of layer 5 from Nb doped hematite with samplings of 100, 1200, and 12800. The results here are representative of other layers and other dopants.

3.2.3 Electrical Conductivity Ensemble Method

Since atomic doping breaks the degeneracy of carrier mobility in each layer, we propose an ensemble method to get an average electrical conductivity by taking the contribution of each layer into consideration,

$$\sigma = \sum_i \sigma_i = e \sum_i^6 n_i \mu_i \tag{3.3}$$

among which n_i and μ_i are the carrier concentration and carrier mobility in each layer. The concentration for each layer is calculated from using equation 3.4, where the probabilities were translated from energies of different configurations by using Boltzmann distribution.

$$n_i = np_i = n\sum_j p_{i,j} \tag{3.4}$$

where n is the total carrier concentration, p_i is the probability of an EP forming on layer i, and $p_{i,j}$ is the probability of forming an EP on site j of layer i and j goes to infinity to simulate the dilute limit condition. The total concentrations for each dopant system were calculated at a representative condition of p_{O_2} at 1 atm and T_S at 1073K. On the other hand, the carrier mobility of each layer can be calculated by following equation 3.5, where energy barrier E_a is obtained from kMC calculations (equation 3.2),[16]

$$\mu = \frac{ea^2 n\tau_0}{4k_B T} e^{-\frac{E_a}{k_B T}} \tag{3.5}$$

among which e is electron charge, a is the EP hopping distance, n is the number of equivalent neighbors and τ_0 is the attempt frequency (168.9 THz^{-1}),[16] $k_B T$ is thermal energy (0.0259 eV at room temperature). All parameters can be found in Table 3.4.

Table 3.4 Parameters for mobility calculations.

Parameters	Values
Electron charge (**e**) (C)	1.6×10^{-19}
EP hopping distance (**a**) (cm)	2.83
Equivalent neighbors (**n**)	3
Attempt frequency ($\boldsymbol{\tau_0}$) (THz^{-1})	168.9
Thermal energy ($\mathbf{k_B T}$) (eV)	0.0259
Energy barrier ($\mathbf{E_a}$) (eV)	It varies

3.3 Energy and Associated Probability Distribution of EP Locating at Different Fe Sites

EP concentration in pristine hematite at $T_S = 1073$ K and $p_{O_2} = 1$ atm is calculated to be 1.47×10^{13} cm^{-3} according to our previous paper,[11] which is used as reference for doped hematite. Three representative dopants, Sn, Ti and Nb, are picked to study how dopants impact the carrier mobility and electrical conductivity in hematite. Sn and Ti are chosen because they are the most well studied group IV dopants, and there are many literature results available for comparison.[2,19] Nb is one of the most well studied group V elements.[20] As mentioned earlier, since the original degeneracy of carrier concentration and carrier mobility in hematite is broken after doping, we proposed an ensemble method to take the contribution of each layer into account to get the average electrical conductivity. In order to compute the carrier concentration in

each layer, we, first of all, calculated the energy distribution of EP locating on different Fe sites (Fig. 3.4a). Overall, the EP energy is reversely proportional to the dopant-polaron distance, which is related to the Coulomb interaction nature between dopant and EP. One thing worth noticing is that Sn and Ti only generate one EP while Nb generates two EPs. The inconsistent number of EPs makes the direct comparison between different dopants unfair. To address this issue, we add one extra positive charge in Nb doped hematite to cancel one EP and leave only one EP in the system. The Nb doped hematite with one extra positive charge is denoted as Nb Q+1 system. On the other hand, no positive or negative charges are added to Sn and Ti doped hematite, they are both neutral, denoted as Sn Q0 and Ti Q0. Then, the probability of EP distributing on different Fe sites is derived based on the Boltzmann distribution (Fig. 3.4b) and normalized to make sure that the probability summation of all data points is equal to 1. The EP concentration in each layer is obtained by summing up the probability of data points in the same layer, multiplied by EP concentration of the whole supercell (equation 3.4). It can be noticed that EPs distribution is layer dependent, and they are easier to form on Fe sites that are close to the dopant, such as those ones in layer 2, 3 and 4 (Note: dopant is substituting the middle Fe site in layer 3). If a probability of 1% is used as a threshold (dashed line in Fig. 3.4b), most data points above the threshold fall into layer 2, 3 and 4. Layers that are further away from the dopant such as layer 1, 5, and 6, have lower probabilities of forming EP.

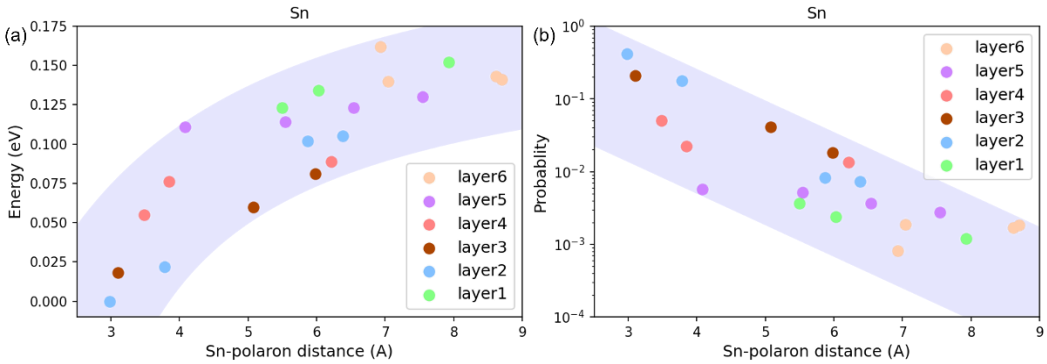

Figure 3.4 EP energy and probability distribution for Sn doped hematite. (a) Energy distribution of EP locating at different sites as a function of Sn-polaron distance. The Coulomb interaction trend is highlighted by the wide strip. (b) Probability distribution of EP locating at different sites as a function of Sn-polaron distance. The wide strip is indicating the inverse relationship between probability and Sn-polaron distance. Dopant is substituting the middle Fe site in layer 3.

3.4 Energy Barriers, kMC, and Carrier Mobility Calculations

The EP transport in pristine hematite is studied first, which is used as a reference for doped hematite. Linear interpolation method is used to obtain the energy barrier due to the advantage of low computational cost. First of all, the IS and FS of EP hopping has to be stabilized, then several intermediate images are obtained by taking a series of ratio between IS structure and FS structure. The image with the highest energy is further relaxed to find the energy barrier. Linear interpolation method gives an EP hopping barrier of 0.11 eV for pristine hematite (Fig. 3.5), consistent with literature reported

values,[15] suggesting that the method is reliable. Based on equation 3.5, the carrier mobility in pristine hematite is 0.056 $cm^2/(V\ s)$.

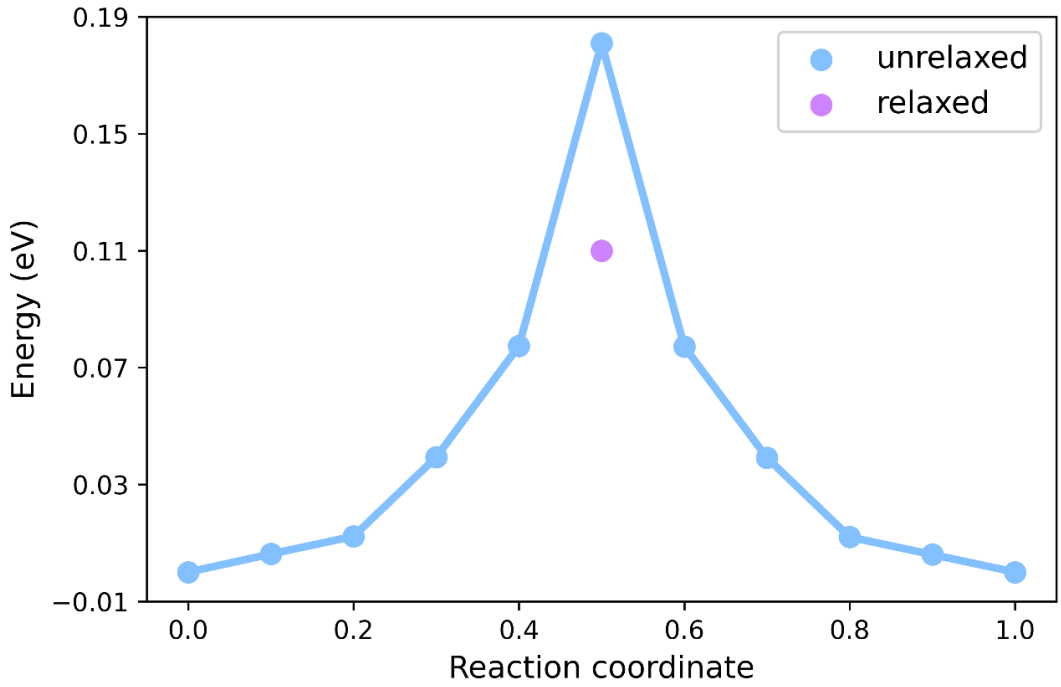

Figure 3.5 Linear interpolation result in pristine hematite. The purple dot is the relaxed energy barrier while other data points are the energy of intermediate images.

In terms of doped hematite, in order to calculate the effective energy barrier and carrier mobility in each layer, all possible EP hopping in each layer are computed, listed in Table 3.1 (Sn doping), 3.2 (Ti doping), and 3.3 (Nb doping). Then kMC method is employed to obtain the effective energy barrier in each layer. First of all, MSD was plotted over time, which is corresponding to diffusion coefficient, Fig. 3.6a and 3.6c. Then, the diffusion coefficient of each layer was fitted over temperature to obtain the

effective energy barrier for each layer according to Arrhenius equation, Fig. 3.6b and 3.6d. After effective energy barrier is obtained, carrier mobility of each layer can be calculated based on equation 3.5. The carrier concentration, effective energy barrier, carrier mobility, and electrical conductivity in each layer for different dopants are listed in Table 3.5. With carrier concentration and carrier mobility of each layer computed, the overall electrical conductivity in the system can be calculated based on equation 3.3. Our computed electrical conductivities for the three dopants are listed in Table 3.6, and some experimental results of the three dopants are also included in the table for comparison. It can be noticed that our calculated results are in a reasonable range of different experimental measured ones, indicating the robustness of our computational methods.

Similar to the layer dependent of EP concentration, the carrier mobility is also layer dependent across all dopants. Layers that are closer to the dopant usually have slower carrier mobility, and carrier mobility gradually recovers to that of pristine value when layers are further away from the dopant. Some interesting qualitative trends among carrier concentrations, carrier mobility and electrical conductivity can be observed. For example, for single dopant, the carrier concentration and carrier mobility trends are opposite, and the electrical conductivity trend follows better with the trend of carrier concentration. This is because the carrier mobility change is relatively small compared to the 2-3 orders of carrier concentrations change across different layers as shown in Table 3.5, therefore, carrier concentration is more dominate in determining the electrical conductivity for single dopant. However, when different dopants are cross

compared, the criteria are different. Both carrier concentration and carrier mobility need to be considered to obtain the correct trend across different dopants. The different criteria is because the carrier concentration across different dopants does not change too much (within one order) and the contribution from carrier mobility cannot be ignored. Overall, the carrier concentration trend is Ti > Nb > Sn, the carrier mobility trend is Ti > Sn > Nb and the electrical conductivity trend is Ti > Sn > Nb.

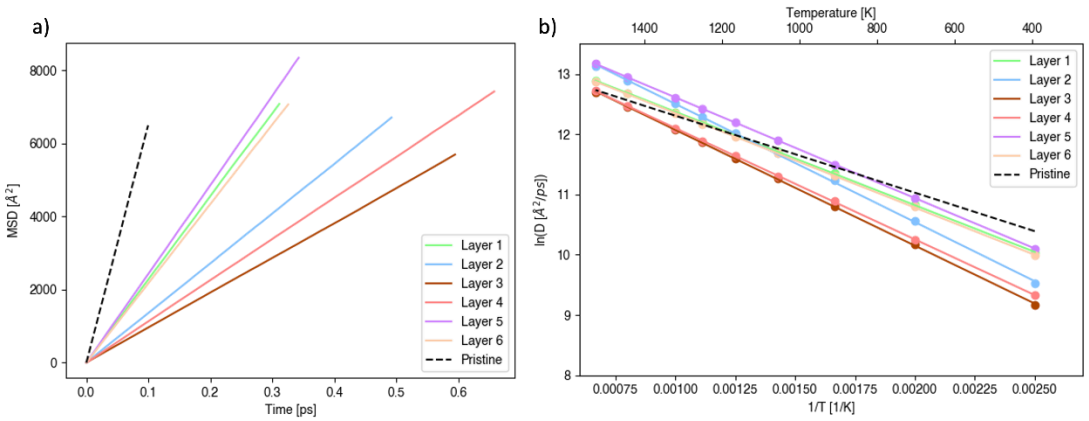

Figure 3.6 Sn doped hematite as a representative example of MSD linearity and Arrhenius relation of diffusion and temperature. a) MSD over time for different layers from kMC simulations. b) Natural log of diffusion as it changes with inverse temperature for different layers. Dopant is always substituting the middle Fe site in layer 3.

Table 3.5 EP hopping properties of each layer for each dopant. Carrier concentration (n_i), effective energy barrier (E_a^{eff}), mobility (μ_i) and conductivity (σ_i) for each layer of each dopant are listed.

Dopant	Layers	n_i (cm^{-3})	E_a^{eff} (eV)	μ_i (cm^2/(V s))	σ_i (S/cm)
Sn	1	3.22×10^{17}	0.132	0.0241	1.24×10^{-3}
	2	2.75×10^{19}	0.169	0.0060	2.63×10^{-2}
	3	1.21×10^{19}	0.165	0.0069	1.34×10^{-2}
	4	3.85×10^{18}	0.158	0.0091	5.60×10^{-3}
	5	7.76×10^{17}	0.144	0.0157	1.95×10^{-3}
	6	2.77×10^{17}	0.134	0.0229	1.01×10^{-3}
Ti	1	4.37×10^{17}	0.137	0.0203	1.42×10^{-3}
	2	8.44×10^{18}	0.160	0.0086	1.16×10^{-2}
	3	1.36×10^{19}	0.156	0.0100	2.17×10^{-2}
	4	2.47×10^{20}	0.160	0.0084	3.34×10^{-1}
	5	2.96×10^{18}	0.147	0.0139	6.57×10^{-3}
	6	5.19×10^{17}	0.131	0.0264	2.19×10^{-3}
Nb	1	2.35×10^{16}	0.138	0.0198	7.45×10^{-5}
	2	1.47×10^{19}	0.186	0.0031	7.20×10^{-3}
	3	5.97×10^{19}	0.198	0.0020	1.87×10^{-2}
	4	2.22×10^{20}	0.191	0.0026	9.27×10^{-2}
	5	2.50×10^{17}	0.149	0.0129	5.18×10^{-4}

Table 3.6 Comparison of our computed for carrier concentration, activation energy, and conductivity with experimental values. NR for not reported. * denotes doner concentration.

Sample	n (cm^{-3})	E_a (eV)	σ (S/cm)
3.0% Sn[exp, 7]	1.6×10^{19}	0.140	0.11
3.0% Sn[ours]	4.5×10^{19}	0.133-0.169	0.05
3.0% Ti[exp, 21]	8.8×10^{19}	0.118	0.57
3.0% Ti[ours]	2.7×10^{20}	0.131-0.160	0.38
3.0% Nb[exp, 20]	5.0×10^{19}	NR	NR
3.0% Nb[ours]	3.0×10^{20}	0.138-0.198	0.12

3.5 Trends across Different Dopants

We are interested in understanding how different dopants impact the electrical conductivity in doped hematite and finding what makes a dopant effective in improving electrical conductivity. To answer these two questions, we started from two potentially promising factors based on our previous experience, Coulomb interactions between dopant and EP and strain by atomic doping. In order to study the Coulomb interaction between dopant and EP, we changed the charge of the dopant by adding positive or negative charge into the supercell. We picked Nb and Sn as examples. For Nb, we simulated Q0 system (two EPs in the supercell) and Q+1 (one positive charge is added, only one EP in the supercell) system to compare interactions between Nb^{4+}-EP and Nb^{5+}-EP. For Sn, we simulated Q0 system (one EP in the supercell) and Q-1 (one negative charge is added, two EPs in the supercell) system to compare interactions between Sn^{4+}-EP and Sn^{3+}-EP. We directly calculated and compared energy barriers for the different charged systems, Fig. 3.7. The energy difference is relatively small

when the charge of dopant changes, usually below 0.2 eV, suggesting that the Coulomb interaction between the dopant and EP is not the main reason governing the energy barriers. One note is that for Sn Q-1 and Nb Q0 systems, some energy barriers are missing because EPs do not tend to form at certain positions.

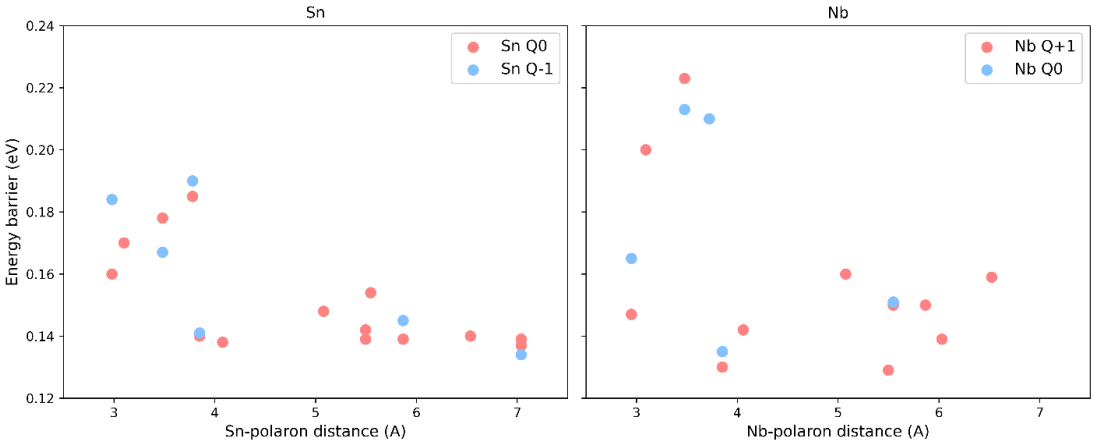

Figure 3.7 EP hopping barrier at different dopant charge states for (left panel) Sn and (right panel) Nb.

Strain effect was then studied by calculating the strain energy of EP locating on different Fe sites. It is computed as a difference of total energy of the doped system with relaxed geometry from the doped system (first relax with dopants, then substitute back Fe atoms to keep the same composition as pristine Fe_2O_3) and with its equilibrium geometry.[22] Strain energy of all data points can be divided into two regions by taking dopant-polaron distance around 4.5 A as a threshold, Fig. 3.8(a). Beyond this threshold, strain energies are relatively stable and fluctuate in an energy range of 0.1 eV. Considering that the strain effect is usually localized, we propose that there is weak

interaction between the dopant and EP when their distance is beyond 4.5 A. To verify the assumption, we calculated strain energy of isolated dopant such as Sn Q+1 system (one positive charge is added into Sn doped hematite supercell and there is only Sn dopant and no EP), and strain energy of EP which is obtained from doing a single-point energy calculation by using the relaxed structure of pristine hematite with one EP. The summed-up energy is represented by the dashed horizontal line in Fig. 3.8(a). It can be noticed that there is some discrepancy between the plateau and the dashed line. We believe that the difference is due to the finite size of supercell as indicated by the much smaller discrepancy between the plateau and the dashed line for $3 \times 3 \times 1$ supercell as shown in the right panel of Fig. 3.9. When the dopant-polaron distance is short, *i.e.*, below the threshold, they are squeezed into a compact space and the strong interaction between them decreases the strain energy to some extent. Similar conclusions can be drawn from observing how energy barriers change with respect to dopant-polaron distance as shown in Fig 3.8(b). Below the threshold, the energy barriers change significantly, however, they stay relatively stable beyond the threshold. The consistent trend between strain energy and energy barriers suggests that focusing on strain is the correct direction to understand the impacts of doping on the electrical conductivity of hematite. Therefore, we dive deeper into this by correlating strain with PES, since PES is intuitive to observe energy barrier change.

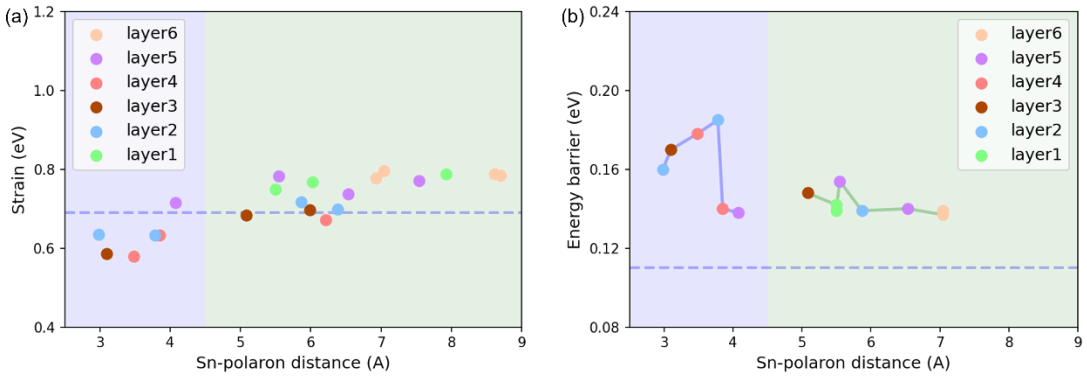

Figure 3.8 Strain and energy barrier as a function of Sn-polaron distance. (a) Strain energy of EP locating at different Fe sites for Sn doped hematite as a function of Sn-polaron distance. (b) EP hopping barriers for Sn doped hematite as a function of Sn-polaron distance.

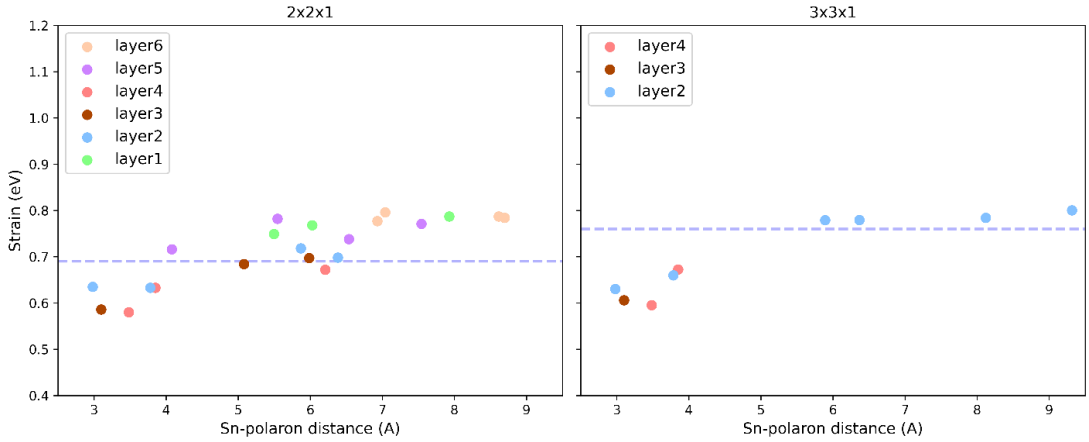

Figure 3.9 Strain energy of EP locating on different Fe sites for Sn doped hematite (left) $2 \times 2 \times 1$ supercell and (right) $3 \times 3 \times 1$ supercell. The dashed line is the summation of strain energy of isolated Sn dopant and strain energy of EP.

Table 3.7 Statistical data for Fe-Fe distances falling into different parts as compared to pristine Fe-Fe distances.

Dopant	Closer (%)	Same (%)	Farther (%)
Ti	6.13	88.65	5.22
Sn	15.77	75.45	8.78
Nb	21.26	68.86	9.87

3.6 Fe-Fe Sublattice Distortion and Potential Energy Surface

We computed all Fe-Fe pair distances of all possible configurations for each dopant, which is another way of directly characterizing strain after atomic doping. Fig. 3.10(a) is the distribution function (g(r)) for all Fe-Fe pair distances in all configurations for the three dopants, while Fig. 3.10(b) is the integrated pair distribution function (PDF) for the three dopants. Ti shows the smallest Fe-Fe pair distance disorder while Nb has the largest, which is consistent with the carrier mobility trend for the three dopants. In addition, these Fe-Fe pair distances are divided into three sections, based on the Fe-Fe pair distances compared to the value in pristine hematite, Table 3.7, “Closer” region (Fe-Fe pair distance shorter than the pristine one by at least 0.01 A), “Same” region (Fe-Fe pair distance falls within an error bar of $\pm$0.01 A compared to the pristine one), and “Farther” region (Fe-Fe bond length longer than the pristine one by 0.01 A). Among the three dopants, Nb has the greatest percentage of

"Farther" section, which means that Nb doped hematite has the most stretched Fe-Fe pair distance compared to the other two dopants. How Fe-Fe pair distance changes energy barrier can be explained by the potential energy surface (PES). As indicated by Fig 3.11 scenario (1), longer Fe-Fe pair distance shifts the PES of IS and FS horizontally and corresponds to a greater energy barrier. On the other hand, Ti has the smallest percentage of "Farther" Fe-Fe pair distances, suggesting that the number of stretched Fe-Fe pair distances is the least among the three dopants. The data in Table 3.7 is consistent the carrier mobility trend observed earlier. The previous observed layer dependence of carrier mobility can also be explained by the result here. For layers that are closer to dopant, the nearby Fe-Fe pair distance is easier to be disrupted and deviate from pristine one, which generates larger EP hopping barrier, unfavorable for carrier mobility.

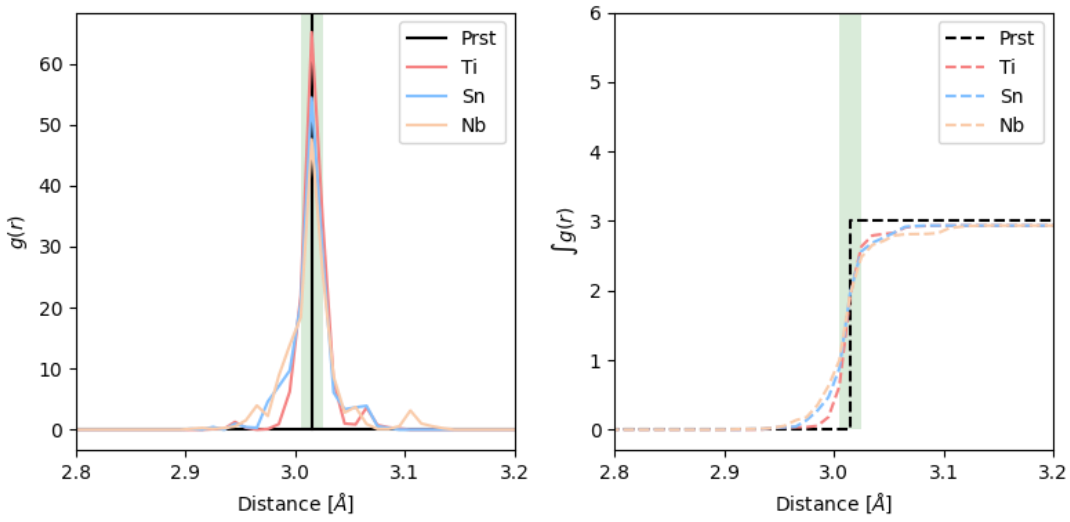

Figure 3.10 Statistical summation of all Fe-Fe distances for all configurations.

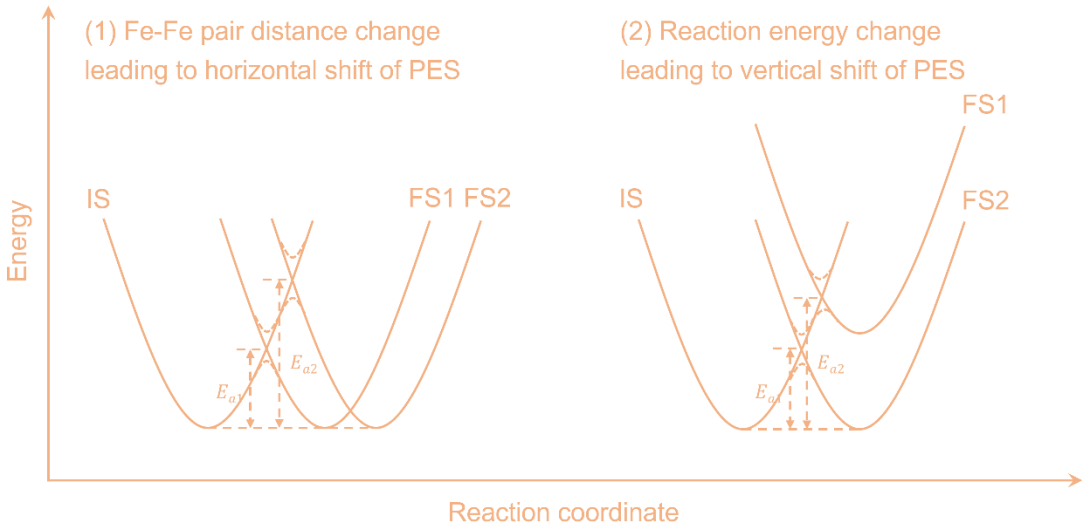

Figure 3.11 Diagram showing a direct correlation between strain/reaction energy and PES. How energy barrier changes in the process is also labeled in the Figure. (a) Fe-Fe pair distance change leading to horizontal shift of PES, (b) Reaction energy change leading to vertical shift of PES.

In addition, the reaction energy change between IS and FS will lead to the vertical shift of PES, further change the energy barrier, as shown in scenario (2) in Fig. 3.11. For example, the PES in the left panel of Fig. 3.13 is much deeper than the PES in the right panel of Fig 3.13, considering when the polaron-polaron distances of both are similar to each other, the much smaller energy barrier in the left panel of Fig. 3.13 is due to the vertical shift of PES in FS. We also fitted energy barriers of all EP hopping against their reaction energies and found there is a linear correlation between energy barrier and reaction energy (Fig. 3.12), consistent with PES analysis in Fig. 3.11 scenario (b). For each dopant, the general information about the reaction energy

between IS and FS can be found from Fig. 3.4. The larger the vertical gap between two nearby same color data points (meaning that they are on the same layer), the larger the reaction energy is, which is not favorable for EP hopping. In fact, the reaction energy can also be correlated to the disorder of Fe sub-lattice, indicated by the relative peak heights in the Fe PDF, which directly corresponds to the trend in mobility (Ti > Sn > Nb). The smaller the Fe-Fe pair distance disorder is, the smaller the reaction energy is (closer to 0), which is beneficial for EP hopping.

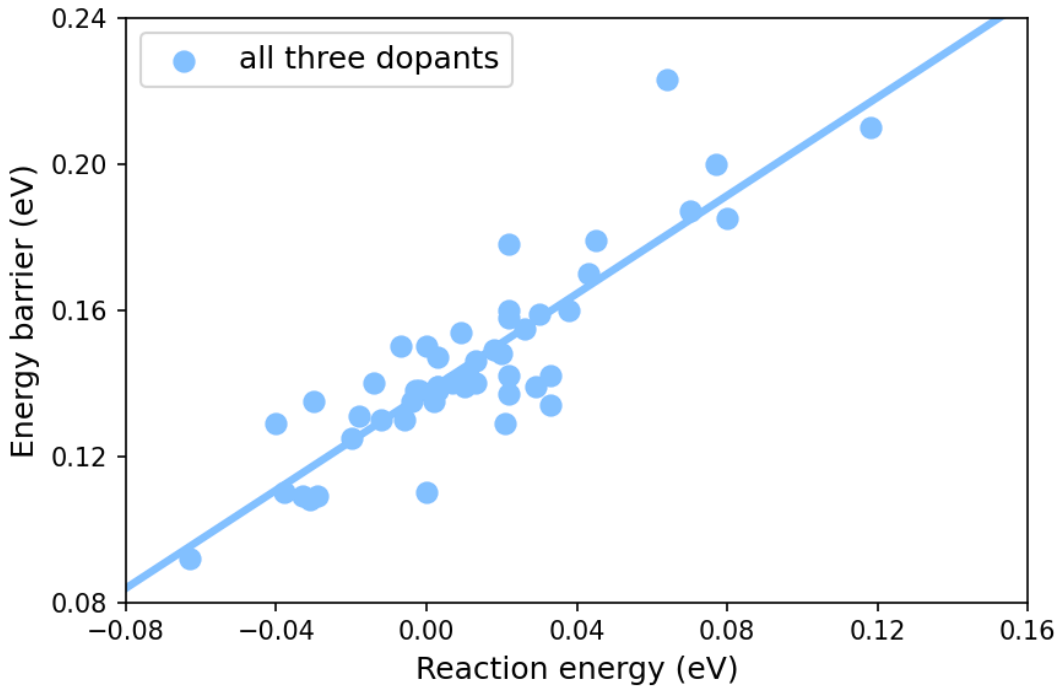

Figure 3.12 Energy barriers as a function of reaction energies between IS and FS. The linear fitting in the figure indicates that energy barrier is correlated to reaction energy.

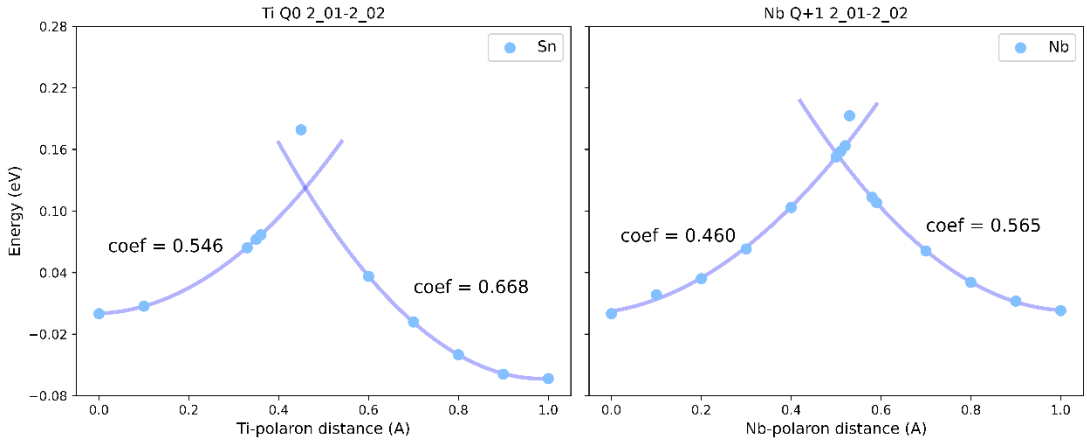

Figure 3.13 Comparison of two selected representative PESs of EP hopping. The "coef" means the coefficient of the fitted parabola. The plot on the left is selected from Ti doped hematite. Q0 means that the system is neutral without adding or removing charge. The plot on the right is selected from Nb doped hematite. Q+1 means that the system has one more positive charge to make sure that there is only one EP for fair comparison with Ti Q0 system. 2_01-2_02 means the EP hops from Fe01 in layer 2 to Fe02 in layer 2. The detailed notation can be found in Fig. 3.3.

3.7 Conclusion

In conclusion, we systematically investigated how dopants affect the carrier mobility and electrical conductivity in hematite. Instead of only focusing on the first EP hopping away from the dopant, we studied all possible EP hopping in the supercell, followed by using kinetic Monte Carlo sampling to find the averaged energy barrier

and carrier mobility in each layer. Considering the strong anisotropy of EP, only carrier mobility in ab plane is considered. Combined with our previous work on how to obtain carrier concentration in hematite, we could obtain the overall electrical conductivity in hematite by taking the contribution of each layer into consideration. The good comparison with experimental measured values indicates the robustness of our computational methods. It was found that doping does not improve carrier mobility, the reason doping improves the electrical conductivity is because of the enhanced carrier concentration. After investigation, we found that structural distortion is the underlying reason for the change of carrier mobility. Among the three dopants studied, Ti shows the highest carrier mobility while Nb has the lowest. This is because Ti generates the lowest percentage of stretched Fe-Fe pair distances while Nb generates the largest percentage, therefore, the former is favorable for EP hopping and the latter is the worst among the three dopants. In addition, the strong disruption of structure will also deviate the reaction energy from the value in pristine hematite. The larger reaction energy is also not favorable for EP hopping. Both Fe-Fe pair distance and reaction energy change can be related to PES to explain the energy barrier change. Therefore, dopants which cause the least structure disorder are more promising for improving the carrier mobility of hematite. Our work herein dives deep into understanding how dopant impacts the carrier mobility and electrical conductivity in hematite and provides realistic guidance to experimentalists about what dopants to choose to optimize the electrical conductivity of hematite and performance of hematite-based device.

Acknowledgements

This work was supported by the National Science Foundation (NSF) under Grant Nos. DMR-2003563 and CHE-1904547. Part of this work was performed under the auspices of the U.S. Department of Energy (DOE) by the Lawrence Livermore National Laboratory under Contract No. DE-AC52-07NA27344. T.J.S. acknowledges the LLNL Graduate Research Scholar Program and funding support from LLNL LDRD 20-SI-004. This research used resources of the Scientific Data and Computing center, a component of the Computational Science Initiative, at the Brookhaven National Laboratory under Contract No. DE-SC0012704; the lux supercomputer at UC Santa Cruz, funded by the NSF MRI grant (No. AST 1828315); the National Energy Research Scientific Computing Center (NERSC), a U.S. Department of Energy Office of Science User Facility operated under Contract No. DE-AC02-05CH11231; and the Extreme Science and Engineering Discovery Environment (XSEDE), which is supported by the NSF (Grant No. ACI-1548562).[23]

Reference

[1] A. B. Murphy, P. R. F. Barnes, L. K. Randeniya, I. C. Plumb, I. E. Grey, M. D. Horne, and J. A. Glasscock, Int. J. Hydrogen Energy **31,** 1999 (2006).

[2] Y. Ling, G. Wang, D. A. Wheeler, J. Z. Zhang, and Y. Li, Nano Lett. **11,** 2119 (2011).

[3] Y. Ling, G. Wang, J. Reddy, C. Wang, J. Z. Zhang, and Y. Li, Angew. Chem. Int. Ed. **51,** 4074 (2012).

[4] M. Li, Y. Yang, Y. Ling, W. Qiu, F. Wang, T. Liu, Y. Song, X. Liu, P. Fang, Y. Tong, and Y. Li, Nano Lett. **17,** 2490 (2017).

[5] Y. Yang, M. Forster, Y. Ling, G. Wang, T. Zhai, Y. Tong, A. J. Cowan, and Y. Li, Angew. Chem. Int. Ed. **55,** 3403 (2016).

[6] C. Franchini, M. Reticcioli, M. Setvin, and U. Diebold, Nat. Rev. Mater. **6,** 560 (2021).

[7] C. M. Tian, W. W. Li, Y. M. Lin, Z. Z. Yang, L. Wang, Y. G. Du, H. Y. Xiao, L. Qiao, J. Y. Zhang, L. Chen, J. Phys. Chem. C **124,** 12548 (2020).

[8] P. Liao and E. A. Carter, J. Appl. Phys. **112,** 013701 (2012).

[9] S. Kerisit and K. M. Rosso, J. Chem. Phys. **127,** 124706 (2007).

[10] Z. Zhou, R. Long, and O. V. Prezhdo, J. Am. Chem. Soc. **141,** 20222 (2019).

[11] T. J. Smart, M. Chen, A. C. Grieder, V. Urena Baltazar, F. Bridges, Y. Li, and Y. Ping, J. Appl. Phys. **130,** 245705 (2021).

[12] N. Iordanova, M. Dupuis, and K. M. Rosso, J. Chem. Phys. **122,** 144305 (2005).

[13] P. Giannozzi, S. Baroni, N. Bonini, M. Calandra, R. Car, C. Cavazzoni, D. Ceresoli, G. L. Chiarotti, M. Cococcioni, I. Dabo, J. Phys.: Condens. Matter **21,** 395502 (2009).

[14] S. L. Dudarev, G. A. Botton, S. Y. Savrasov, C. J. Humphreys, and A. P. Sutton, Phys. Rev. B **57,** 1505 (1998).

[15] T. J. Smart and Y. Ping, J. Phys.: Condens. Matter **29,** 394006 (2017).

[16] N. Adelstein, J. B. Neaton, M. Asta, and L. C. De Jonghe, Phys. Rev. B **89,** 245115 (2014).

[17] K. F. Garrity, J. W. Bennett, K. M. Rabe, and D. Vanderbilt, Comput. Mater. Sci. **81,** 446 (2014).

[18] F. Wu and Y. Ping, J. Mater. Chem. A **6,** 20025 (2018).

[19] Z. Fu, T. Jiang, Z. Liu, D. Wang, L. Wang, and T. Xie, Electrochim. Acta **129,** 358 (2014).

[20] C. Sanchez, K. D. Sieber, and G. A. Somorjai, J. Electroanal. Chem. Interf. Electrochem. **252,** 269 (1988).

[21] B. Zhao, T. C. Kaspar, T. C. Droubay, J. McCloy, M. E. Bowden, V. Shutthanandan, S. M. Heald, and S. A. Chambers, Phys. Rev. B **84,** 245325 (2011).

[22] T. J. Smart, V. U. Baltazar, M. Chen, B. Yao, K. Mayford, F. Bridges, Y. Li, and Y. Ping, Chem. Mater. **33,** 4390 (2021).

[23] J. Towns, T. Cockerill, M. Dahan, I. Foster, K. Gaither, A. Grimshaw, V. Hazlewood, S. Lathrop, D. Lifka, G. D. Peterson, Computing in Science & Engineering **16,** 62 (2014).

Chapter 4 – Experimental Measurements of Electrical Conductivity of Doped Hematite

Abstract

First-principles density functional theory (DFT) calculations are coupled with experimental approaches to understand the impact of atomic doping to the electrical conductivity of hematite. Our previous DFT calculations have already predicted how atomic doping changes the carrier concentration, carrier mobility, and electrical conductivity, therefore, in this section, experimental approaches are designed to verify the predicted results. Different synthesis methods such as spin coating, post-processing, hydrothermal reaction, etc., are elaborated and the pros and cons of each method are discussed, followed by different characterization techniques. Then different electrical conductivity measurement methods are compared starting from four-point probe conductivity measurement. Some alternative methods are also proposed such as photoelectrochemical water splitting and electrochemical impedance spectroscopy if the quality of thin film for four-point probe conductivity measurement cannot be satisfied. The experimental measurement results can verify our previous calculated DFT results and validate the robustness of our computational methods.

4.1 Introduction

Hematite is a promising material for many different energy conversion and storage applications due to advantages such as low cost, high abundance, and good chemical stability. However, the electrical conductivity of hematite is very low, for example, the carrier mobility of hematite is about 6-7 orders lower compared to Si, which is already very insulating.[1] The poor electrical conductivity of hematite strongly hinders hematite to be widely applied in different applications. For example, if the electrical conductivity of hematite is improved, then the performance of hematite-based device for photoelectrochemical (PEC) water splitting and supercapacitors should boost. Atomic doping has been one of the most used approaches to improve the electrical conductivities of hematite. For example, Wang *et al.* synthesized Ti doped hematite and found a boost in photocurrent.[2] Li *et al.* intentionally doped Sn into hematite and achieved an outstanding OER photocurrent density of 2.2 mA cm^{-2} at 0.23 V vs Ag/AgCl.[3] Although many works have been done in the field to understand the effect of atomic doping in hematite, the question of how atomic doping impacts electrical conductivity of hematite still has not been well answered yet.

Coupling first-principles DFT calculations with experimental approaches has been proven to be able to solve challenging problems. Previously first-principles DFT calculations have been employed to understand the following questions: (1) how does doping bottleneck affect carrier concentration in hematite? (2) How does synthesis conditions change the carrier concentration in doped hematite? (3) How does atomic doping impact the carrier mobility and electrical conductivity in hematite? Therefore,

how carrier concentration, carrier mobility and electrical conductivity of hematite change with respect to atomic doping have been predicted.

Herein, experimental approaches are employed to verify previous DFT calculations. Different approaches are proposed to measure the electrical conductivity of hematite. Four-point probe conductivity measurement is the best approach to obtain the energy barrier and conductivity. However, the four-point probe conductivity measurement of hematite thin film is challenging considering since some criteria have to be satisfied. First of all, the prepared thin film has to be uniform and continuous. A thin film stacked with random nanostructures is not the ideal for four-point probe conductivity measurement. In addition, cracks should also be avoided since they will divide the film into incontiguous islands. Second, the film cannot be too thin otherwise it is difficult to obtain a conductivity measurement result. Third, hematite has to be doped to improve the electrical conductivity otherwise the electrical conductivity of pristine hematite is too low to be measured. Fourth, considering the strong anisotropic carrier mobility in different directions, special attention has to be paid to the growth direction of hematite.[1,4] Hematite structure grown along c-axis is not favorable for conductivity measurement. Last, conductive metals have to be deposited onto thin hematite film to create good contact between probes and the hematite surface, otherwise the metal-insulating interface gives a very large contact resistance. Except the direct four-point probe conductivity measurement, some alternative methods can also be used to indirectly measure the electrical conductivity. For example, at dark conditions for PEC water splitting measurement, the current density at different applied

potential is strongly related to the electrical resistance of the hematite thin film. The smaller solution resistance and charge transfer resistance are an indication for the smaller electrical resistance. Electrochemical impedance spectroscopy (EIS) can also be used to extract electrical conductivity information. The two intercepts in Nyquist plot can tell us the solution resistance and charge transfer resistance, which is strongly related to electrical resistance of the thin film. Another part that is covered in this section is different synthesis methods for hematite such as spin-coating method, post-processing method, hydrothermal reaction method, etc. The pros and cons of each method will be discussed. This work provides detailed experimental plan for how to measure the electrical conductivity of hematite, which will serve as a direct and confident evidence for previous DFT calculations.

4.2 Synthesis

Several different synthesis methods will be discussed, and the pros and cons of each synthesis method will be mentioned.

4.2.1 Spin Coating

7.00 g of iron (III) nitrate ($Fe(NO_3)_3 \cdot 9H_2O$) and 10.00 g of citric acid ($C_6H_8O_7$) are dissolved in 20 mL DI H_2O. The solution is heated at 60-70 ^oC and kept under stirring throughout the process until all salts are dissolved. 6.70 g ethylene glycol is added to the solution, and further heated at 70 ^oC for 30 minutes. In the process, the ferric ions are chelated by citric acid and ethylene glycol will trigger the

polyesterification reaction. 10 mL solution is taken out of the batch after cooling down and concentrated to 5 mL by evaporating. Then desired amount of dopant precursor (depending on doping percentage) is added into the concentrated solution, followed by adding 1.50 mL anhydrous ethanol and 1.00 mL isopropyl alcohol in order. The final solution is stored in a refrigerator at ~2 ^{o}C for overnight.

For the spin coating part, 50 μL solution is dropped onto a 1.5×1.5 cm^2 FTO substrate or quartz substrate. Then the substrate spins at 500 rpm for 5 seconds followed by 7000 rpm for another 30 seconds. This process is repeated until 1 mL solution is added. After spin coating, the substrate is annealed in air at 550 ^{o}C for 30 min first, then ramped up to 800 ^{o}C for another 30 min. The ramping rate is around 40 ^{o}C/min. The first soaking stage at 550 ^{o}C is to convert Fe precursor to Fe_2O_3, and the further annealing at 800 ^{o}C is to make sure that dopant diffuse into the crystal structure of hematite. The spin coating and annealing process together is called one cycle. The procedures are shown in Fig. 4.1.[5]

Spin coating method can give a uniform and high-quality film, as shown in Fig. 4.2 In addition, the thickness of the thin film can be tuned by repeating several cycles of spin coating and annealing. However, it's very easy to form cracks on the surface during annealing, as shown in Fig. 4.2, which could be detrimental to the conductivity measurement, which can be possibly solved by changing ramping rate or depositing another layer of thin layer on the top of current one.

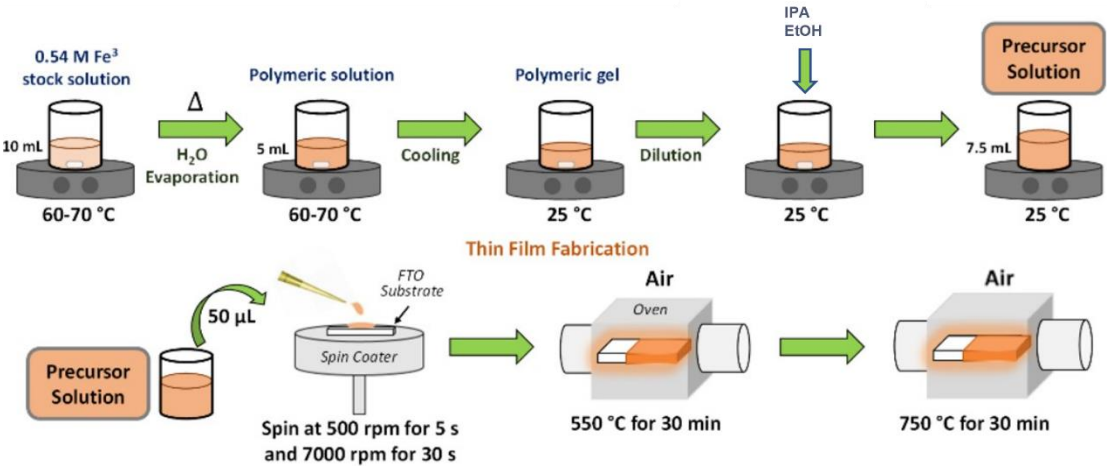

Figure 4.1 Scheme showing the procedures of using spin coating method to prepare hematite thin films.

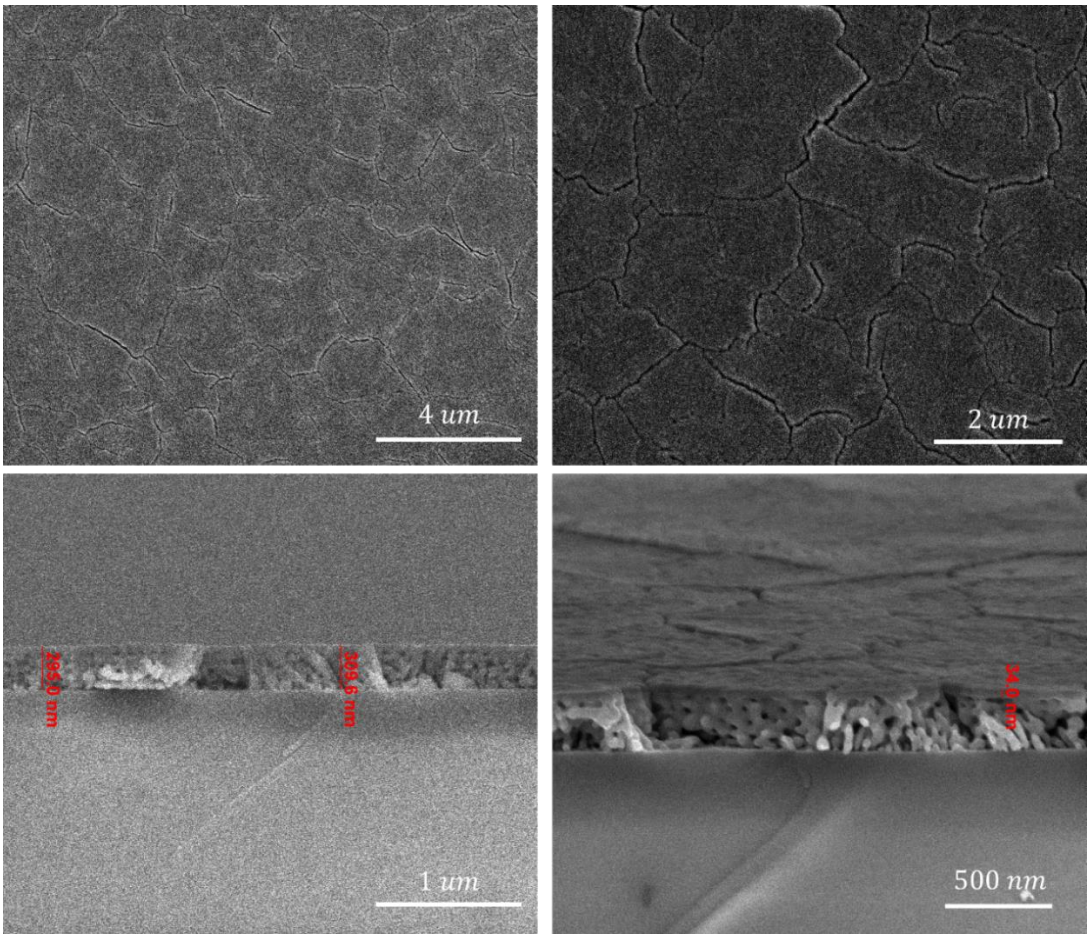

Figure 4.2 SEM images of 1% Sn doped hematin thin film on quartz prepared by spin coating method.

4.2.2 Post-processing

This method involves two processes, hydrothermal reaction to synthesize FeOOH film on substrate, and then drop-cast dopant precursor solution on FeOOH film followed by annealing to achieve doping. In hydrothermal reaction, 4.05 g ferric chloride hexahydrate ($FeCl_3$ $6H_2O$) and 8.50 g sodium nitrate ($NaNO_3$) are dissolved in 100 mL DI H_2O. After the powders are totally dissolved, 350 µL concentrated HCl is added into the solution to adjust the pH to ~1.5.[6] The solution is transferred to a 120 mL autoclave, a 4.5 × 3.0 cm^2 FTO or sapphire is added into the autoclave as well. If the substrate is FTO, then the conducting side should face down. The autoclave is then heated at 95 ^oC for 4 hours. After the autoclave is cooled down, the substrate is retrieved from the liner and rinsed with DI H_2O and ethanol, successively. Then the dopant precursor solution such as $SnCl_4$ EtOH solution is drop-casted onto the FeOOH film with desired amount. After that, the substrate is annealed in air at 550 ^oC for 30 min first to convert FeOOH to hematite, then the temperature is further ramped up to 800 ^oC or higher to achieve doping. The whole post-processing method flow is shown in Fig. 4.3.

The main issue of using this method for preparing thin film for four-point probe conductivity measurement is that it is very easy to form island shape morphology in

hydrothermal reactions. The discontinuous thin film is unfavorable for electrical conductivity measurement.

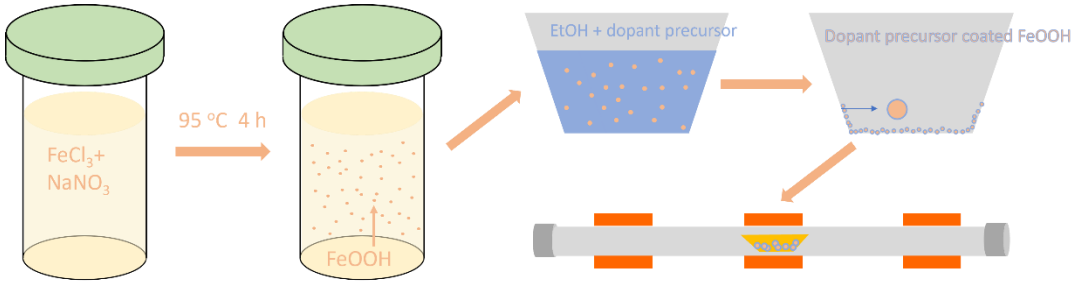

Figure 4.3 Procedures of using post-processing method to prepare doped hematite powders.

4.2.3 Hydrothermal Reaction

This method is very similar to previous post-processing method, as shown in Fig. 4.4.[6] The biggest difference is that the doping is achieved by adding dopant precursor during hydrothermal reaction process. For example, in order to achieve Ge doping, except adding the previous described chemicals, $GeCl_4$ EtOH solution is also added into the solution. After the hydrothermal reaction, we assume that Ge is incorporated into FeOOH thin film. Then the dopant incorporated thin film is annealed in air with the same procedures described before. SEM images of Ge doped hematite thin film are shown in Fig. 4.5.

The advantage of using this method is that doping can be achieved in the hydrothermal reaction process directly, there is no extra procedures required to incorporate dopant into FeOOH structure. However, with this method, the doping

concentration in FeOOH or hematite can be possibly different from the doing concentration in the reaction solution since not all dopants can enter FeOOH film. In addition, it's very easy to form oxides with this method, which is detrimental to conductivity measurement.

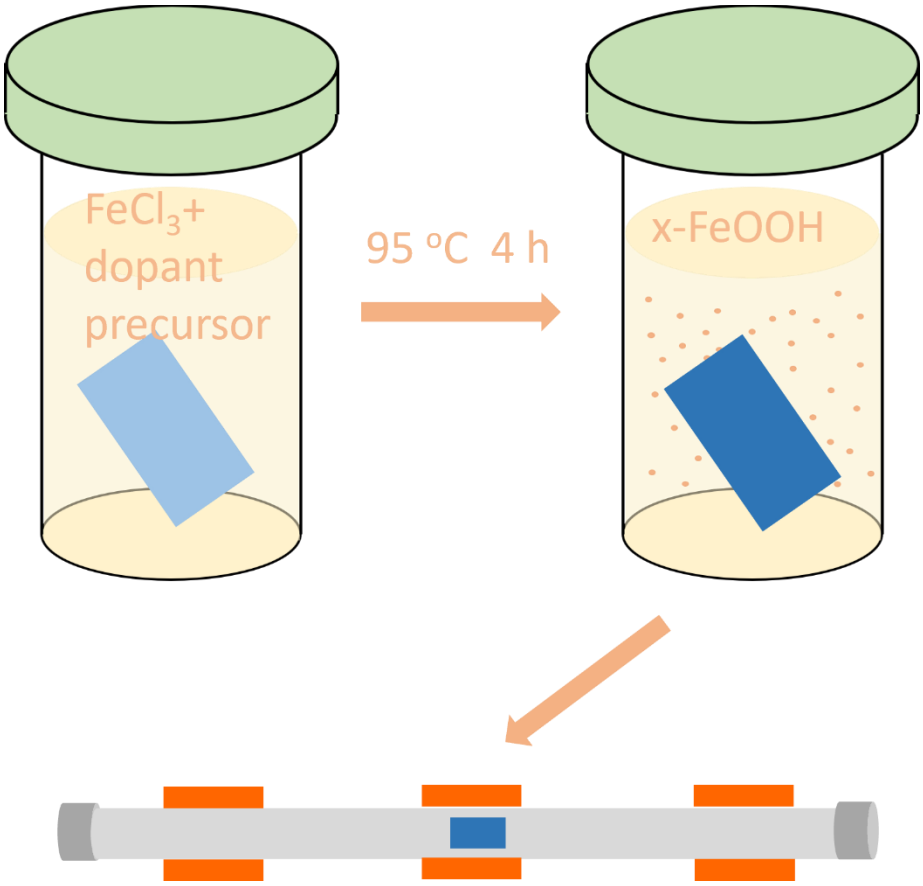

Figure 4.4 Procedures of using hydrothermal reaction method followed by annealing to prepare doped hematite samples.

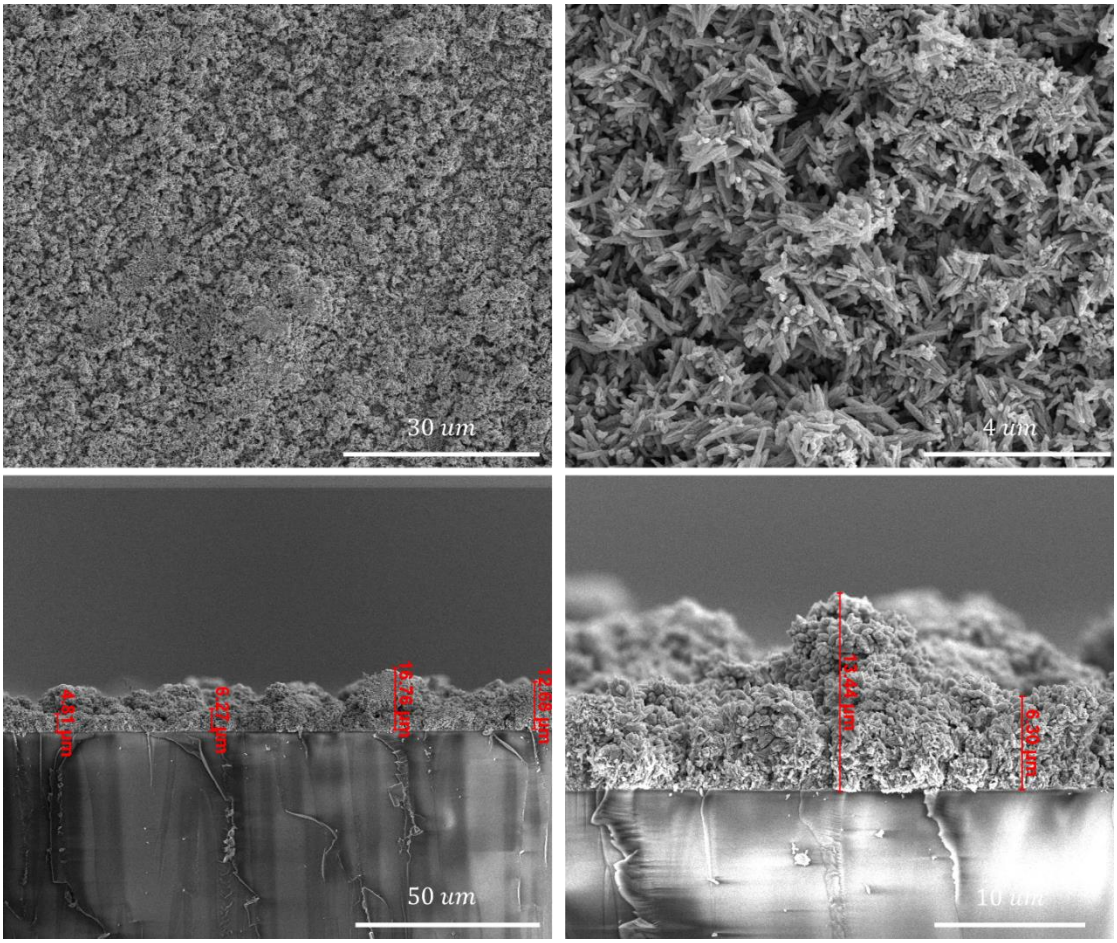

Figure 4.5 SEM images of 0.5% Ge doped hematite thin film on FTO substrate by using hydrothermal reaction method.

4.2.4 Pulsed Laser Deposition

In this method, doped hematite powders are prepared first, then pulsed laser is used to deposit make hematite thin films. Taking Sn doping as an example, Fe_2O_3 powders are mixed well with SnO_2 powders in desired ratio and ground for 30 minutes, and subsequently heated at 800 ^oC for 8 hours. After cooling, the powders were ground

again and pressed in a stainless-steel mold and sintered in air at 1200 °C for 12 h. The pressed pellet is ablated with laser at a repetition rate of 5 Hz and an energy density of 1.2 J/cm^2. Films with a thickness of ~ 40 nm were grown in 0.10 Torr oxygen at a substrate temperature of 550 °C and cooled to room temperature in the same O_2 pressure.[7]

4.3 Characterization

Different characterizations will be used to characterize the synthesized materials. First of all, scanning electron microscopy (SEM) is used to check the morphology of thin film grown on substrate. Island shape morphology of hematite thin film forms on the surface of substrate after hydrothermal reaction method, as shown in Fig. 4.6(a). Second, x-ray diffraction (XRD) will be used to characterize the phase and crystal structure of synthesized powders and films. Three main peaks at 24^o, 33^o, and 35^o are expected, corresponding to (012), (104) and (110), as shown in Fig. 4.6(b).[7] If the doping concentration is high, then it is also possible to observe the phase of dopant oxide. For example, Tian *et al.* observed the peak corresponding to that of SnO_2 for 3 % Sn doped hematite powders.[7] Raman spectroscopy can also be used to check the identity of synthesized powders and films, *i.e.*, four oxygen-based vibrations at 227, 246, 293, and 300 cm^{-1} and three iron-based vibrations at 411, 496, and 612 cm^{-1}.[8] In the end, X-ray absorption spectroscopy (XAS) will be used to check the local structure and coordination information after atomic doping, as well. For example, we used XAS

to measure the structure of 0.1% and 1.0% Sn doped hematite, Fig. 4.6(c). The plot for 0.1% Sn shows a fit to the hematite structure and a good agreement is obtained with a slight contraction of the Sn−O pairs and a slight expansion of the Sn−Fe pairs. At 1% Sn, the EXAFS changes significantly. Although the first two peaks are very similar, the region from 3−3.8 Å is quite different, particularly the shape of the phase (fast oscillating function), and a dip develops near 3.3 Å. These data cannot be fit to the hematite structure. The data suggest that there is another peak present; in the fit shown in the lower panel of Fig. 4.6(c), one of the Fe neighbors at ~3.7 Å is replaced with a Sn atom, forming a Sn−Sn pair. This leads to the excellent fit shown in the lower panel.[9]

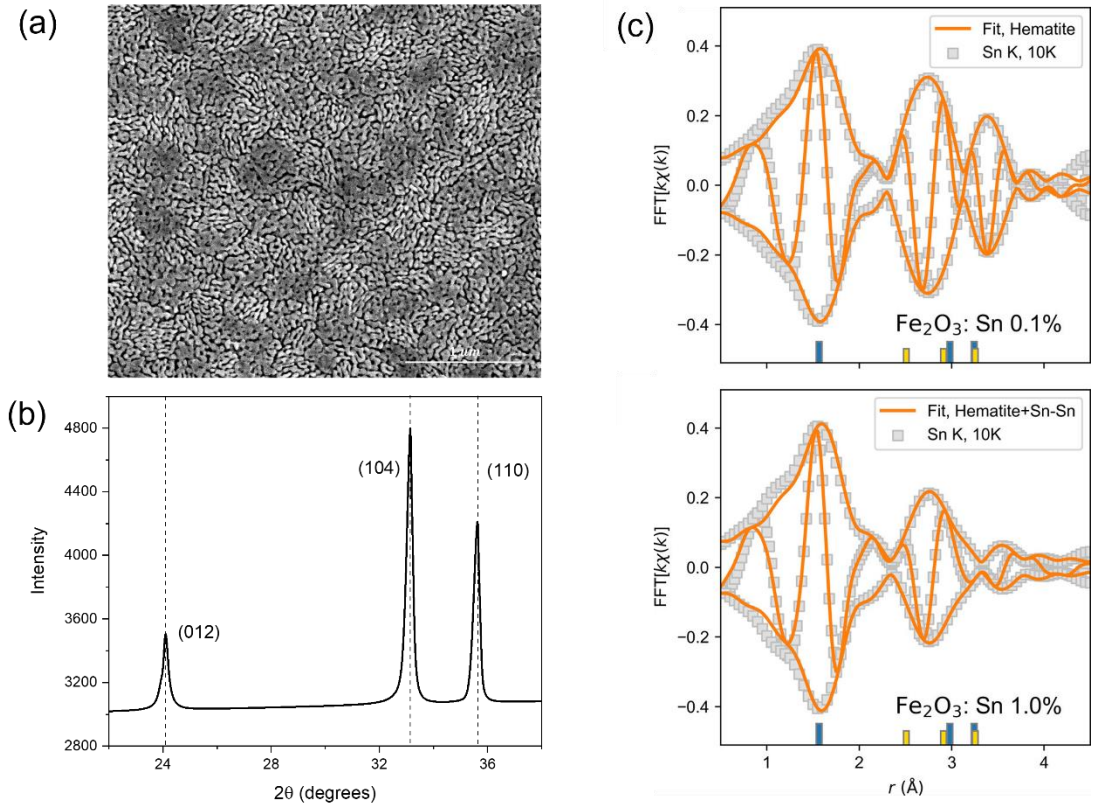

Figure 4.6 Characterizations of hematite. (a) SEM images of pristine hematite grown on the surface of FTO by using hydrothermal reaction method. (b) XRD image of pristine hematite. (c) EXAFS r-space data at the Sn K edge for (a) 0.1% and (b) 1% Sn in Fe_2O_3 at 10 K. Fourier transform range, 3.5−13 $Å^{-1}$; fit range in r-space, 1.1−4.2 Å for both plots.

4.4 Conductivity Measurements

Different methods for measuring the electrical conductivity of hematite will be discussed. The pros and cons of each method will be mentioned.

4.4.1 Four-point Probe Conductivity Measurement

Four-point probe conductivity measurement is the most direct method to obtain the electrical conductivity of hematite. The electrical conductivity of the thin film will be measured at different temperatures, then by fitting the electrical conductivity over temperature through the Arrhenius equation, the effective energy barrier of electron polaron hopping and further mobility can be obtained. For example. Zhang *et al.* employed four-point probe instrument to measure the electrical conductivity of $BiVO_4$ and found that the energy barrier of electron polaron hopping decreases from 557 meV to 382 meV after it is doped by 2% Mo.[10] Fig. 4.7 is an illustrative scheme showing the setup of four-point probe conductivity measurement. If the sample is thick enough compared to the probe interval, then we consider the sample as bulk, then we assume a

spherical protrusion of current passing from the outer probe tips.[11-13] The differential resistance is:

$$\Delta R = \rho\left(\frac{dx}{A}\right) \tag{4.1}$$

where ρ is electrical resistance and A is area. Then the resistance can be obtained by doing integration between the inner probe tips (where the voltage is measured):

$$R = \int_{x_1}^{x_2} \rho \frac{dx}{2\pi x^2} = \frac{\rho}{2\pi}\left(-\frac{1}{x}\right)\Big|_{x_1}^{x_2} = \frac{1}{2s}\frac{\rho}{2\pi} \tag{4.2}$$

where probe spacing is uniformly s. Due to the superposition of current at the outer two tips, $R = V/2I$, we can derive the following equation:

$$\rho = 2\pi s\left(\frac{V}{I}\right) \tag{4.3}$$

If instead, the film thickness (t) is much less than the distance between probes, then the equation will be changed to:[14]

$$\rho = \frac{\pi t}{ln2}\frac{V}{I} \tag{4.4}$$

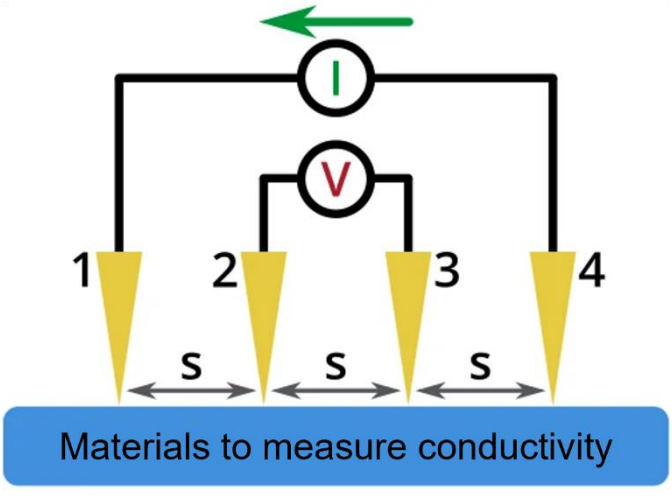

Figure 4.7 The setup of four-point probe conductivity measurement.

4.4.2 EIS

EIS is another possible technique to obtain the electrical conductivity of hematite. Compared to four-point probe conductivity measurement, EIS is the response of the system to the applied alternating current (AC) potential, among which electrical conductivity information about the material can be obtained. Usually there are many different models to simulate the real system, one of the most used is Randles model, which includes a solution resistance (R_S), a charge transfer resistance (R_{ct}) and a double layer capacitance (C_{dl}). The C_{dl} is in parallel with the R_{ct}, and then in serial with R_S. The equivalent circuit for the Randles model is shown in Fig. 4.8a. Due to the simplicity of Randles model, it is also often used as starting point for other more complex models. Nyquist plot is the most used plot for recording EIS information, in which the left side of the plot is high frequency region while the right side of the plot is low frequency region. Fig. 4.8b is a representative Nyquist plot of Randles cell model.[15] The R_S is the intercept at the high frequency side while the intercept at the low frequency side is the summation of R_S and R_{ct}. Therefore, the diameter of the semicircle represents the R_{ct}. R_{ct} is strongly related to the electrical conductivity of samples, the smaller the R_{ct} is, usually the high electrical conductivity is.

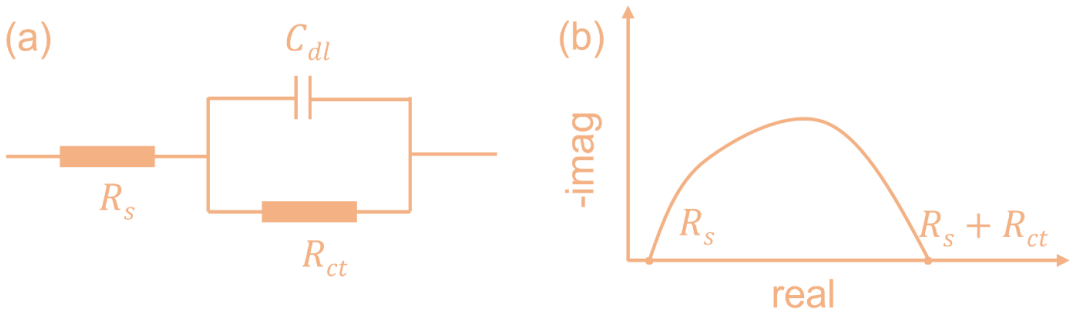

Figure 4.8 Randles model. (a) Simplified Randles cell schematic diagram. (b) An example of Nyquist plot for Randles cell model.

4.4.3 PEC Measurement

PEC measurement is another possible approach to get a sense of electrical conductivity of hematite. For example, by looking at the current-time response to different samples, we could qualitatively compare the electrical conductivities of different samples. One prerequisite of using current-time curve to compare the electrical conductivity of different samples is that the samples should be prepared in the same recipe and different samples' morphology and light absorption should stay roughly the same. For example, in Fig. 4.9, the four different samples are prepared with the same recipe and their morphology and light absorption are roughly the same, therefore, we can conclude that 0.5% Sn doped hematite sample should have the highest electrical conductivity among these four samples.

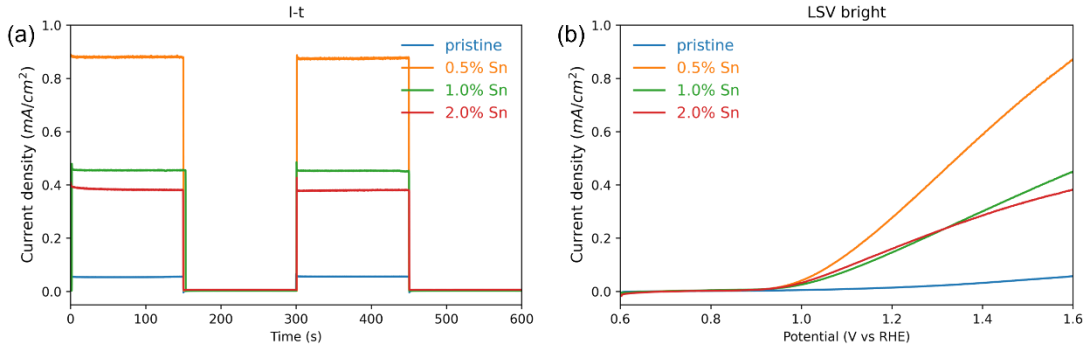

Figure 4.9 PEC measurements of Sn doped hematite. (a) Current-time response and (b) LSV measurements of four different samples, pristine hematite, 0.5% Sn doped hematite, 1.0% Sn doped hematite and 2.0% Sn doped hematite. The current-time measurement was conducted at 1.6 V vs RHE and the electrolyte is 1 M NaOH solution.

4.5 Conclusion

Obtaining the electrical conductivities of doped hematite is critical to verify the first-principles DFT calculation results. In this section, we discussed different methods of synthesizing hematite, then transitioned to how to use different characterizations to probe different information. In the end, different electrical conductivity measurement methods were discussed. Four-point probe measurements are the most direct approach to get the energy barrier and conductivity information of samples. However, four-point probe conductivity measurement usually require a high quality thin film. For example, thin films have to be continuous and uniform, and films cannot be too thin, etc. If such high-quality thin film cannot be obtained and four-point probe measurement is not feasible, then some alternative methods can be used, such as EIS or PEC measurements.

Prerequisites of using these alternative approaches include similar preparation recipe, similar morphology, and light absorption, etc. A consistent experimental measurement results and first-principles DFT predictions could provide convincing and strong explanations to how doping impacts the electrical conductivities of hematite.

Acknowledgements

This work was supported by the National Science Foundation (NSF) under Grant Nos. DMR-2003563 and CHE-1904547.

References

[1] N. Iordanova, M. Dupuis, and K. M. Rosso, J. Chem. Phys. **122,** 144305 (2005).

[2] G. Wang, Y. Ling, D. A. Wheeler, K. E. N. George, K. Horsley, C. Heske, J. Z. Zhang, and Y. Li, Nano Lett. **11,** 3503 (2011).

[3] M. Li, Y. Yang, Y. Ling, W. Qiu, F. Wang, T. Liu, Y. Song, X. Liu, P. Fang, Y. Tong, Nano Lett. **17,** 2490 (2017).

[4] K. M. Rosso, D. M. A. Smith, and M. Dupuis, J. Chem. Phys. **118,** 6455 (2003).

[5] K. C. Bedin, B. Mouriño, I. Rodríguez-Gutiérrez, J. B. S. Junior, G. T. d. Santos, J. Bettini, C. A. R. Costa, L. Vayssieres, and F. L. Souza, Chinese J. Catal. **43,** 1247 (2022).

[6] Y. Ling, G. Wang, D. A. Wheeler, J. Z. Zhang, and Y. Li, Nano Lett. **11,** 2119 (2011).

[7] C. M. Tian, W. W. Li, Y. M. Lin, Z. Z. Yang, L. Wang, Y. G. Du, H. Y. Xiao, L. Qiao, J. Y. Zhang, L. Chen, J. Phys. Chem. C **124,** 12548 (2020).

[8] Y. Liu and R. D. L. Smith, ACS Appl. Mater. Interfaces **14,** 6615 (2022).

[9] T. J. Smart, V. U. Baltazar, M. Chen, B. Yao, K. Mayford, F. Bridges, Y. Li, and Y. Ping, Chem. Mater. **33,** 4390 (2021).

[10] W. Zhang, F. Wu, J. Li, D. Yan, J. Tao, Y. Ping, and M. Liu, ACS Energy Lett. **3,** 2232 (2018).

[11] F. M. Smits, Bcl] Syst. Tech. J. **37,** 711 (1958).

[12] A. Uhlir Jr, Bcl] Syst. Tech. J. **34,** 105 (1955).

[13] S. Dieter, *Semiconductor material and device characterization* (IEEE Press; Wiley, Piscataway NJ; Hoboken N.J., 2006).

[14] R. S. Waremra and P. Betaubun, E3S Web Conf. **73** (2018).

[15] J. E. B. Randles, Discuss. Faraday Soc. **1,** 11 (1947).

Chapter 5 – Outlook

In the past several decades, the development of first-principles DFT calculations has been really fast owing to two reasons: (1) the development of exchange-correlation functional, which makes it possible to compute the properties of materials accurately with a reasonable computation cost. (2) the development of computing power over the world, which makes it possible to compute bigger and more complex system.[1] However, there has always been a gap between coupling first-principles DFT calculations with experimental approaches to understand the properties of materials. For example, researchers are used to conduct experiments first, and seek theoretical approaches later to help explain the observed results if the experimental result are good. Although this collaboration mode works in many scenarios and has helped the understanding of many materials, it has many drawbacks. For example, human bias is very easy to be applied in the computational process to obtain the desired results for explaining experimental observations. In addition, this collaboration mode cannot fully utilize the advantages of first-principles DFT calculations, *i.e.*, theoretical simulation is a relative cheap and efficient approach to do large scale sample screening compared to doing experiments. To overcome the limitations of aforementioned collaboration mode, we have been developing more efficient and interactive collaboration mode of coupling first-principles DFT calculations with experimental approaches to explore the properties of materials. In this dissertation paper, we take hematite as an example, first of all, employed first-principles DFT calculations to predict how atomic doping impacts the electrical conductivities of hematite, then

followed by experimental approaches to verify previous simulation results. The advantages of doing in this way is that we can fully utilize the advantages of first-principles DFT for screening different possible dopants, without investing too much time and cost for testing different dopants. Theoretically, we have used first-principles DFT calculations to answer the following questions: (1) how does dopant clustering change the carrier concentration in hematite? (2) How does synthesis temperature change the carrier concentration in doped hematite? (3) How does atomic doping impact the carrier mobility and electrical conductivity of hematite? Experimentally, we have been synthesizing different doped hematite, characterizing them with different techniques and using different methods to measure the conductivity.

In the future, one possible following topic is to study how does the combination of different dopants impact the carrier concentration, carrier mobility and electrical conductivity of hematite? This topic is interesting since different dopants would have different effects for improving the electrical conductivities of hematite. For example, if we combine one dopant with smaller ionic size than Fe^{3+} such as Ti with another dopant with larger ionic size than Fe^{3+} such as Sn, the strain effect from the two different dopants could cancel each other, then possible higher carrier concentration could be achieved with higher doping concentration. On the other hand, the canceled strain from different dopants could decrease the Fe-Fe pair distance disorder in hematite structure, which could be beneficial for improving the carrier concentration according to our previous computational results.

Another interesting topic is to use machine learning (ML) to study the effect of atomic doping to the electrical conductivity of hematite. Traditional first-principles approaches have limitations when dealing with many-polaron system, and when effects such as dopant clustering and combination of different dopants are considered, it is very challenging to employ first-principles DFT calculations to study these effects due to too many possibilities. In this case, ML could be an ideal tool to take into account all different factors. For example, Birschitzky *et al.* utilized a DFT+ML protocol to explore millions of polaron configurations for two systems, oxygen deficient rutile TiO_2 (110) and Nb doped $SrTiO_3$ (001). The new protocol is able to individuate ground-state polaron patterns, predict new possible polaron configuration that has not been visited before and efficiently determine the optimal charge distribution for each polaron configuration.[2] These possible follow-up projects can further help us understand how atomic doping impacts the electrical conductivity of hematite. With this domain of knowledge clarified, other strategies such as nanostructure engineering can be coupled to further boost the performance of hematite-based device for different applications.

Reference

[1] M. Chen, T. J. Smart, S. Wang, T. Kou, D. Lin, Y. Ping, and Y. Li, J. Mater. Chem. A **8,** 8783 (2020).

[2] Viktor C. Birschitzky, Florian Ellinger, Ulrike Diebold, Michele Reticcioli, and C. Franchini, arXiv (2022).